On the role of whistler-mode waves in electron interaction with dipolarizing flux bundles

JGR Space Physics

RESEARCH ARTICLE
10.1029/2022JA030265

On the Role of Whistler-Mode Waves in Electron Interaction With Dipolarizing Flux Bundles

A. V. Artemyev[1], A. I. Neishtadt[2], and V. Angelopoulos[1]

[1]Department of Earth, Planetary, and Space Sciences, University of California, Los Angeles, Los Angeles, CA, USA, [2]Department of Mathematical Sciences, Loughborough University, Loughborough, UK

Key Points:

- An approach for evaluation of electron flux dynamics around plasma injections is proposed
- Scattering of injected electrons by whistler-mode waves affects electron adiabatic heating
- Scattering of injected electrons by whistler-mode waves may account for observed electron precipitation

Correspondence to:

A. V. Artemyev,
aartemyev@igpp.ucla.edu

Citation:

Artemyev, A. V., Neishtadt, A. I., & Angelopoulos, V. (2022). On the role of whistler-mode waves in electron interaction with dipolarizing flux bundles. *Journal of Geophysical Research: Space Physics*, *127*, e2022JA030265. https://doi.org/10.1029/2022JA030265

Received 6 JAN 2022
Accepted 19 MAR 2022

Abstract The magnetotail is the main source of energetic electrons for Earth's inner magnetosphere. Electrons are adiabatically heated during flow bursts (rapid earthward motion of the plasma) within dipolarizing flux bundles (concurrent increases and dipolarizations of the magnetic field). The electron heating is evidenced near or within dipolarizing flux bundles as rapid increases in the energetic electron flux (10–100 keV); it is often referred to as injection. The anisotropy in the injected electron distributions, which is often perpendicular to the magnetic field, generates whistler-mode waves, also commonly observed around such dipolarizing flux bundles. Test-particle simulations reproduce several features of injections and electron adiabatic dynamics. However, the feedback of the waves on the electron distributions has been not incorporated into such simulations. This is because it has been unclear, thus far, whether incorporating such feedback is necessary to explain the evolution of the electron pitch-angle and energy distributions from their origin, reconnection ejecta in the mid-tail region, to their final destination, and the electron injection sites in the inner magnetosphere. Using an analytical model we demonstrate that wave feedback is indeed important for the evolution of electron distributions. Combining canonical guiding center theory and the mapping technique we model electron adiabatic heating and scattering by whistler-mode waves around a dipolarizing flux bundle. Comparison with spacecraft observations allows us to validate the efficacy of the proposed methodology. Specifically, we demonstrate that electron resonant interactions with whistler-mode waves can indeed change markedly the pitch-angle distribution of energetic electrons at the injection site and are thus critical to incorporate in order to explain the observations. We discuss the importance of such resonant interactions for injection physics and for magnetosphere-ionosphere coupling.

1. Introduction

The thermal (0.1–5 keV) and energetic (5–300 keV) electron populations in the Earth's magnetotail arise by the energization of initially cold ≤100 eV electrons from the shocked solar wind or the ionosphere. An investigation of the relative contributions of different energization mechanisms is important, because electrons play a crucial role in magnetosphere-ionosphere coupling (Khazanov et al., 2018; Ni et al., 2016; Nishimura et al., 2020) and are responsible for magnetotail current sheet currents (Artemyev, Petrukovich, et al., 2011; Kamaletdinov et al., 2020; Lu et al., 2019; Runov et al., 2006). The two main electron acceleration mechanisms are adiabatic heating and wave-particle interactions. The former applies to heating by the convection (dawn-dusk) electric field during earthward transport, be it quasi-steady and large scale (Artemyev et al., 2012; Lyons, 1984; Zelenyi et al., 1990) or impulsive and localized (Birn et al., 2012, 2013; Fu et al., 2011, 2013; Gabrielse et al., 2012, 2014). The latter applies to field-aligned acceleration by kinetic Alfven waves (Artemyev, Rankin, & Blanco, 2015; Cheng et al., 2020; Damiano et al., 2015, 2016), lower-hybrid waves (Cairns & McMillan, 2005), and various electrostatic solitary waves (Lotekar et al., 2020; Vasko et al., 2015), as well as by electromagnetic whistler-mode waves (whistlers; Breuillard et al., 2016; Le Contel et al., 2009; Malykhin et al., 2021; Panov et al., 2013; Zhang et al., 2018) and electron cyclotron harmonic waves (Ni et al., 2012; Zhang & Angelopoulos, 2014; Zhang et al., 2021). Electron adiabatic heating and wave-electron interactions operate on different time scales, thus they are modeled using different approaches.

The average convection electric field in the Earth's magnetotail is ∼0.05 mV/m (Angelopoulos et al., 1993; Sergeev et al., 1996), and corresponds to a ∼10 to 50 km/s earthward convection for an equatorial $B_z \in [1, 10]$ nT in the middle tail (hereinafter we use the GSM coordinate system). Therefore, the typical time-scale of electron transport from $\sim 30R_E$ to $\sim 10R_E$ is ∼1.5 hr. This time-scale would be an order of magnitude smaller, ∼10 min, for fast plasma flows transporting electrons earthward with velocity ∼200 to 500 km/s (Angelopoulos

et al., 2013; Liu et al., 2014; Runov, Angelopoulos, Zhou, et al., 2011). During their earthward transport, most electrons crossing the equator are bouncing between magnetic mirror points adjacent to the current sheet. This bounce motion affects the efficiency of adiabatic heating (Artemyev, Zelenyi, Petrukovich, & Nakamura, 2011; Birn et al., 2012; Fu et al., 2012; Tverskoy, 1969; Zelenyi et al., 2013). The typical time-scale of electron bounce motion is $\sim 4L/v \sim 2\,\text{second}/\sqrt{h}$ where $L \sim 1R_E$ is the typical magnetotail current sheet half-thickness and h is the electron energy in kiloelectron volt. Therefore, accurate modeling of adiabatic electron heating requires resolving electron dynamics with a temporal resolution better than 1 s. This can be readily achieved with test particle simulations in dynamic electromagnetic fields obtained from global MHD simulations (see examples in Ashour-Abdalla et al., 2011; Birn et al., 2013; Eshetu et al., 2018, 2019; Sorathia et al., 2018) or from analytical approximations of spacecraft observations (see examples in Gabrielse et al., 2016, 2017; Zaharia et al., 2000). However, to model wave-electron interactions, which for classical cyclotron resonance occur within a fraction of an electron gyroperiod, ~1 to 10 ms, a much higher temporal resolution (smaller time step) is required, ~0.1 to 1 ms. This is computationally challenging for a large ensemble of electrons and for the long integration times needed to capture the full electron evolution (tens of minutes). Thus, electron interactions with waves are mostly modeled by solving the diffusion equation, which is mainly applicable in a strong background magnetic field, such as that of the near-Earth magnetotail (Ni et al., 2016) and inner magnetosphere (see reviews by Li & Hudson, 2019; Shprits et al., 2008; Thorne et al., 2021 and references therein). Merging these two approaches (test particle simulations to follow adiabatic heating and solving the diffusion equation to track the effect of waves on the electron distributions) has been proposed, mostly for applications to the inner magnetosphere (e.g., Elkington et al., 2019; Lukin, Artemyev, & Petrukovich, 2021; Michael et al., 2021), but it has yet to be implemented.

It is particularly desirable to incorporate both adiabatic evolution and wave-electron interactions on electron energization in the near-Earth magnetotail: there, the most intense fluxes of energetic electrons are associated with plasma injections (Fu et al., 2013; Gabrielse et al., 2014, 2019). These are characterized by strong adiabatic heating of electrons trapped within the strong magnetic field of the dipolarizing flux bundle (Birn et al., 2013, 2014; Gabrielse et al., 2016; Lu et al., 2016; Zaharia et al., 2000). Such heating is predominantly anisotropic and mostly increases the transverse electron energy component, creating anisotropic electron populations (Fu et al., 2012; Motoba et al., 2020; Runov et al., 2013). Instabilities of these anisotropic populations are responsible for the generation of intense whistlers (Fu et al., 2014; Malykhin et al., 2021; Tao et al., 2011), as observed around dipolarizing flux bundles (Grigorenko et al., 2020; Khotyaintsev et al., 2011; Le Contel et al., 2009; Zhang et al., 2018, 2019). Electron resonant interaction with such whistlers can result in rapid electron acceleration, but also efficient pitch-angle scattering. Since adiabatic heating strongly depends on electron pitch angle (Birn et al., 2012; Lyons, 1984; Tverskoy, 1969), such pitch-angle scattering by whistlers is expected to affect the final electron heating and distribution function anisotropy.

There are two main regimes of electron resonant interaction with whistlers: electron diffusion by low-amplitude waves and nonlinear resonant interactions including phase bunching and phase trapping (see reviews by Karpman, 1974; Shapiro & Sagdeev, 1997). Diffusion is well described by quasi-linear theory (Drummond & Pines, 1962; Vedenov et al., 1962) initially developed for whistlers (Andronov & Trakhtengerts, 1964; Kennel & Petschek, 1966; Trakhtengerts, 1963) and later generalized to systems with electron bounce motion (Lyons et al., 1972). The basic characteristics of this theory, that is, the pitch-angle and energy diffusion rates, can be evaluated from measured whistler wave properties (e.g., Albert, 2008; Glauert & Horne, 2005; Mourenas et al., 2012; Shprits & Ni, 2009; Summers et al., 2007) and incorporated into the Fokker-Planck diffusion equation describing the evolution of electron fluxes (see reviews by Lyons & Williams, 1984; Ni et al., 2016; Schulz & Lanzerotti, 1974; Shprits et al., 2008; Thorne et al., 2021 and references therein). Theoretical estimates of these diffusion rates show that diffusive electron scattering around dipolarizing flux bundles can be quite effective (Ghaffari et al., 2021; Khotyaintsev et al., 2011). However, the observed whistler wave intensity is often sufficiently large to allow nonlinear resonant interactions, that may change electron pitch-angle and energy much faster than quasi-linear diffusion (see discussions of these two regimes in Allanson et al., 2020; Artemyev et al., 2019; Gan et al., 2020). The basic characteristics of nonlinear resonant interaction models are the pitch-angle and energy changes due to phase bunching (e.g., Albert, 2002; Allanson et al., 2021; Bell, 1984) and phase trapping (e.g., Demekhov et al., 2006; Omura et al., 2007), and the probability of phase trapping (e.g., Neishtadt, 1975; Shklyar, 1981). These characteristics can be evaluated using observed wave properties (see examples in Artemyev, Neishtadt, et al., 2021; Vainchtein et al., 2018) and can be incorporated into a non-diffusive master equation providing the evolution of electron fluxes (see examples in Artemyev, Neishtadt, Vasiliev, &

Mourenas, 2018; Furuya et al., 2008; Hsieh et al., 2020; Omura et al., 2015). In the present study, we focus on the inclusion of such nonlinear interaction effects into the test-particle simulation scheme. In Section 5 we consider approaches for the future inclusion of diffusive effects.

A way to include effects of resonant wave-particle interaction into test particle simulations was proposed in Tao et al. (2008), where electron diffusion traditionally described by the Fokker-Planck equation was modeled with a set of stochastic differential equations. The idea is to use characteristics of the master (e.g., Fokker-Planck) equation as electron trajectories in phase space, and add diffusion in the form of random electron pitch-angle/energy variations. The analog of the Fokker-Planck equation for systems with nonlinear wave-particle interactions is the master equation including integral operators describing large pitch-angle/energy changes due to the phase trapping (see examples of such equations in Artemyev, Neishtadt, Hietala, et al., 2017; Artemyev, Neishtadt, Vasiliev, et al., 2017; Hsieh & Omura, 2017b; Omura et al., 2015; Vainchtein et al., 2018). Artemyev et al. (2020b) described a set of mapping equations that represent the characteristics of such a master equation. In this study we will modify the mapping approach of Artemyev et al. (2020b) to include nonlinear resonant effects into the test particle electron trajectories describing electron adiabatic heating. The proposed approach will then be applied to a simulation of electron energization around the dipolarizing flux bundle with characteristics typical for plasma injections.

This article consists of four main sections and a conclusion section. In Section 2 we describe our model of adiabatic electron heating. This model is based on the canonical theory of adiabatic invariants and differs slightly from the more widespread models using the noncanonical theory (see discussion in the review by Cary & Brizard, 2009). The basic elements of the canonical theory are reviewed in Appendix A and in Neishtadt and Artemyev (2020). In Section3 we describe the inclusion of wave-particle resonant effects into the test particle simulation. Further description of this approach can be found in Appendices B and C and in Artemyev et al. (2020b); Artemyev, Neishtadt, Vasiliev, et al. (2021); Artemyev, Neishtadt, Zhang, et al. (2021). In Section 4, we apply the model of adiabatic electron heating including wave-particle interactions to plasma injections observed by the Time History of Events and Macroscale Interactions during Substorms (THEMIS) mission (Angelopoulos, 2008). There we also compare model results of electron scattering into the loss-cone with electron precipitation observations by the low-altitude CubeSat ELFIN (Angelopoulos et al., 2020). In Section we discuss possible generalizations of the model. Finally, in Section 6 we briefly summarize the main conclusions of this study.

2. Adiabatic Electron Dynamics

In this section we consider adiabatic dynamics of non-relativistic electrons (with magnetic moment conservation, $\mu = \text{const}$) in the magnetotail's magnetic field in the presence of a moving dipolarizing flux bundle. The goal is to derive equations of motion for the electron gyrocenter's fast bouncing along magnetic field lines and slow cross-field drift due to gradient effects. The most common approach for the zero-order description of the gyrocenter motion is the non-canonical guiding center theory (see Cary & Brizard, 2009; Morozov & Solov'ev, 1966; Northrop, 1963 and references therein). Although this theory introduces the magnetic moment μ as an adiabatic invariant of motion, this invariant is not incorporated further in the Hamiltonian description of the motion as a canonical variable. The resultant non-canonical guiding center equations are adequate for the description of electron dynamics in large-scale electromagnetic fields (e.g., those generated by global MHD simulations, see Eshetu et al., 2018; Ukhorskiy et al., 2011). However, incorporating effects of electron-scale wave perturbations to the electron motion using such guiding-averaged equations is not straightforward. Because our final goal is to describe effects of electron resonant scattering by whistlers on electron interaction with a dipolarizing flux bundle, we need to derive a canonical set of guiding center equations (Gardner, 1959; Neishtadt & Artemyev, 2020). In this canonical set of Hamiltonian equations μ is a Hamiltonian variable, which is considered conserved (invariant) in the absence of waves and its conservation is violated when wave-particle interactions occur. We will see that the canonical guiding center theory approach is quite useful for investigating electron dynamics in the presence of both large-scale magnetic field gradients and electron-scale waves. However, in this approach, the canonical Hamiltonian variables responsible for electron cross-field drift are not Cartesian (spatial) coordinates. These variables are Euler potentials (Stern, 1970), generally used for the description of magnetic field configurations (Birn, 1989; Birn et al., 1977), but much more rarely used to describe electron dynamics

(see examples in Cary & Brizard, 2009). Therefore, the background magnetic field should be expressed in Euler potentials to be included into equations of motion. Below, in Section 2.1 we describe such a background magnetic field configuration, and in Section 2.2 we show that the adiabatic electron dynamics using this approach has all the effects of electron drifts and adiabatic heating.

2.1. Background Magnetic Field Model

We start with a 2D magnetotail current sheet configuration, whose generalized formulation relies on a single component of the vector potential $\mathbf{A} = A(x, z)\mathbf{e}_y$ (Schindler, 1975; Schindler & Birn, 1978). We next incorporate a dipolarizing flux bundle as a B_z enhancement, localized in the (x, y) equatorial plane (Gabrielse et al., 2016). Although such a B_z-enhancement changes significantly the current sheet thickness (i.e., it changes the current sheet configuration in the (x, z) plane; Liu et al., 2013; Nakamura et al., 2004), we do not include this effect in order to simplify the description of the electron motion. In the (x, z) plane, the current sheet embedding dipolarizing flux bundle can be modeled as a simple field configuration:

$$\begin{aligned} A &= -\bar{B}L\cdot\ln\left(\frac{1}{l(x)}\cosh\left(\frac{z\cdot l(x)}{L}\right)\right)\\ B_x &= -\frac{\partial A}{\partial z} = \bar{B}l(x)\tanh\left(\frac{z\cdot l(x)}{L}\right)\\ B_z &= \frac{\partial A}{\partial x} = \bar{B}\varepsilon\frac{l'}{l}\left(1-\left(\frac{z\cdot l(x)}{L}\right)\tanh\left(\frac{z\cdot l(x)}{L}\right)\right)\end{aligned} \tag{1}$$

where $\bar{B}$ is the typical magnetic field magnitude, $\varepsilon = L/L_x$ is the ratio of the current sheet thickness L and the typical scale of the magnetotail inhomogeneity along x, $l' = dl/d(\varepsilon x/L)$ and

$$l(x) = \frac{L}{-\varepsilon\cdot(x+x_0)}\left(1+h_f R\cdot\tanh\left(\frac{X}{R}\right)\right) \tag{2}$$

where x_0 represents the range of the B_z variation along x in the absence of the dipolarizing flux bundle. The dipolarizing flux bundle is described by the second part of Equation 2. The B_z-enhancement's relative amplitude is h_f, the bundle size is R (this is the spatial scale of the magnetic field enhancement), and X is the relative distance to the bundle: $X = x - x_{0f}$ for a stationary 1D bundle located at x_{0f}. It follows that $X = x - x_{0f} - v_f t$ for a bundle moving earthward with a constant speed v_f. Figure 1a shows a set of $B_z(x)$ profiles in $z = 0$ plane at different x_{0f}. Although we do not describe the sharp leading boundary of the dipolarizing flux bundle (Nakamura et al., 2002, 2004; Runov, Angelopoulos, Zhou, et al., 2011; Sitnov et al., 2009), we can model adequately the spatial localization of the B_z enhancement. Figure 1b shows a set of 2D distributions of $B(x, z)$ field magnitude with overplotted magnetic field lines (that are $A = \text{const}$ lines). For such a magnetic field configuration, the Euler potentials are $\alpha = A/\bar{B}$ and $\beta = y$ with $\mathbf{B} = \bar{B}\nabla\beta\times\nabla\alpha$ (Birn, 1989; Birn et al., 1977).

Let us now replot the magnetic field magnitude B as a function of the field-aligned coordinate s and equatorial vector potential $A(x, 0)$. Figure 1c shows $B(s)$ profiles for several equatorial x values (i.e., for three fixed values of A corresponding to those equatorial x values), whereas Figure 1d shows $B(A)$ profile for $s = 0$, that is, at the equator (A is monotonically decreasing with absolute distance $|x|/L$). These profiles show that $B(s)$ can generally be approximated by some combination of polynomial and exponential functions, and that $B(A)$ for $s = 0$ can be fitted as $B \sim \exp(A/A_R)$. Therefore, we can approximate the magnetotail configuration with an embedded dipolarizing flux bundle as:

$$\begin{aligned} B &= \bar{B}f_b(s)G_b(A), \quad f_b(s) = a_0\frac{s^2}{s^2+a_1^2} + \exp\left(s^2/a_2^2\right)\\ G_b(A) &= G_0\exp\left(\frac{A-A_0}{L\bar{B}}\right)\cdot\left(1+G_f\exp\left(-\frac{(A-A_{0f})^2}{A_R^2}\right)\right)\end{aligned} \tag{3}$$

where we modify the $B(s)$ dependence to include the effect of the very strong dipole field in the near-Earth region (this would guarantee that most electrons will be reflected near Earth and do not escape from the magnetotail, as it should be, given the $\lesssim 2°$ loss-cone in the magnetotail plasma sheet; see, e.g., Zhang et al., 2015). Figure 1e

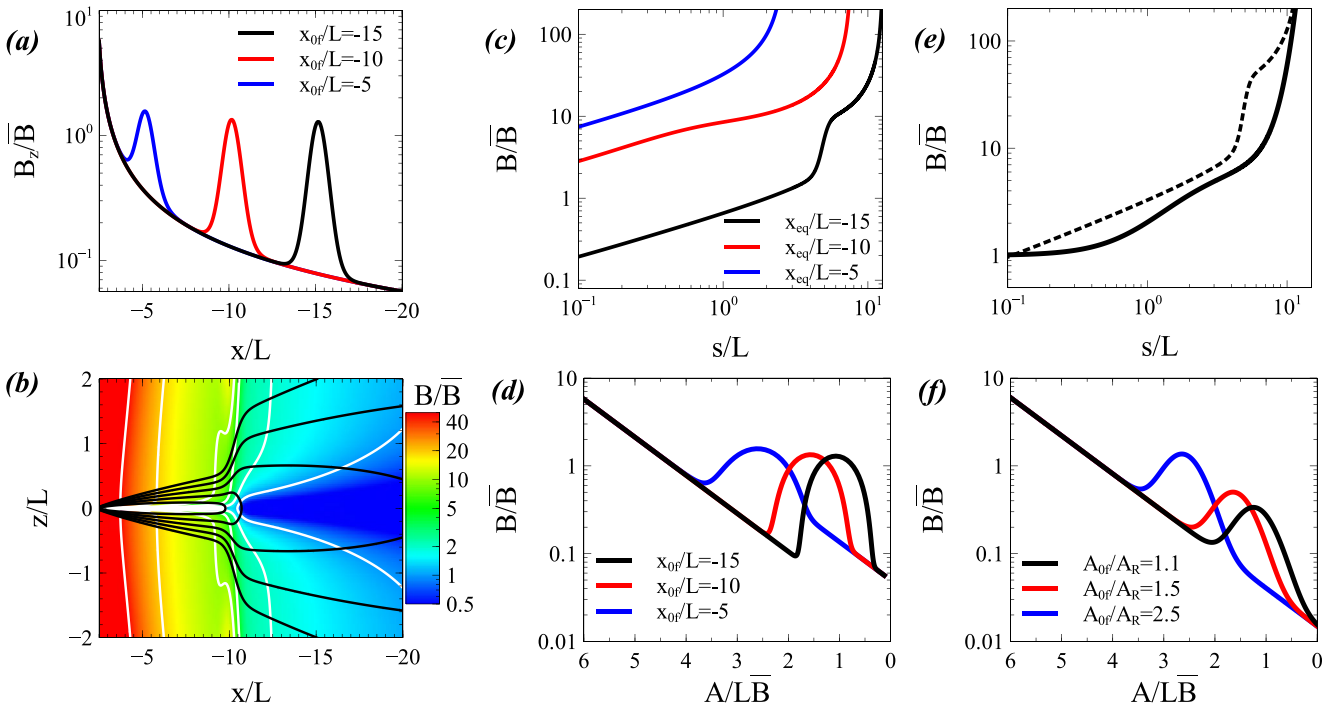

Figure 1. (a) Profiles of $B_z/\bar{B}$ magnetic field given by Equation 1 for $z = 0$, $\varepsilon = 1/20$, $h_f = 5$, and three bundle normalized distances: $x_{0f}/L = (-5, -10, -15)$. (b) $B(x, z)/\bar{B}$ given by Equation 1 for $\varepsilon = 1/20$, $h_f = 5$, and $x_{0f}/L = -10$. Black lines show magnetic field lines, defined as: $A = \text{const}$. (c) Magnetic field magnitude $B/\bar{B}$ along three magnetic field-lines with the same equatorial crossings as in (a). (d) Equatorial magnetic field magnitude as a function of $A/L\bar{B}$ for the same parameters as in (a). (e) Magnetic field magnitude $B/\bar{B}$ along magnetic field-line given by Equation 3 with $a_0 = 5$, $a_1 = 2$, and $a_2 = 5$. Dashed curve show $B/\bar{B}$ from (c) with the normalization to the equatorial value. (f) Equatorial magnetic field magnitude as a function of $A/L\bar{B}$ given by Equation 3 with $G_0 = 6$, $A_0/L\bar{B} = 6$, $G_f = 6$, $A_R = L\bar{B}/2$, and three values of A_{0f} =(1.1, 1.5.2.5).

shows $f_b(s)$, whereas Figure 1f shows $B(A, 0)$. Both functional forms are good representations of the original magnetic field from Figures 1c and 1d). To localize the dipolarizing flux bundle in the dawn/dusk direction (along the Y coordinate), we generalize the G_b function as:

$$G_b(A, Y, t) = G_0 \exp(A - A_0) \cdot \left(1 + G_f \exp\left(-\frac{(A - A_{0f})^2}{A_R^2} - \frac{(Y - Y_{0f})^2}{R^2}\right)\right) \quad (4)$$

Figure 2 shows a set of 2D distributions of the field magnitude, B in the (A, s) and (A, Y) planes, for different locations of the dipolarizing flux bundle. This configuration includes all needed properties of the magnetotail current sheet with the moving dipolarizing flux bundle, and can be used for an investigation of electron adiabatic motion.

2.2. Electron Adiabatic Heating

In Appendix A we have derived the guiding center Hamiltonian for non-relativistic electrons (mass m, charge $-e$) moving in the strong magnetic field ($\mu = \text{const}$):

$$H = \frac{1}{2m} p_\parallel^2 + \mu\Omega_0(s, A, A - cE_f t, Y) \quad (5)$$

where $(s, p_\parallel)$ are the conjugate variables of field-aligned coordinate and momentum, respectively; $\mu = h\sin^2\alpha_{eq}/\Omega_0(0, A_{init}, Y_{init})$ is the electron magnetic moment, conserved and determined by the initial coordinates, equatorial pitch-angle α_{eq} and energy h; and $\Omega_0 = eB(s, A, Y)/mc$ is the electron gyrofrequency. The factor $A - cE_f t$ with the constant eclectic field E_f describes the front motion, that is, the magnetic field reconfiguration with time. Note that μ's conjugate, the gyrophase angle, does not appear in the Hamiltonian, consistent with the fact that μ

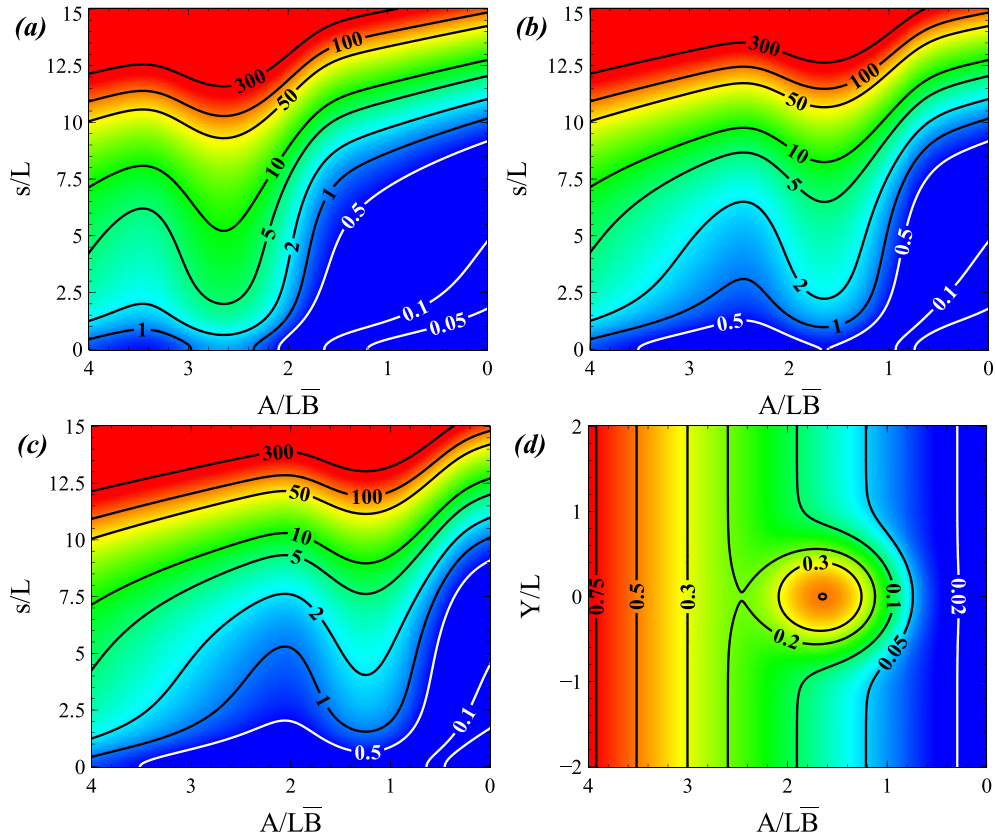

Figure 2. 2D $B/\bar{B}$ plot in the (A, s) plane for three A_{0f} values [2.5, 1.5 and 1.1 for (a), (b), and (c), respectively], and in the (A, Y) plane for $A_{0f} = 1.5$ (d). System parameters are the same as in Figure 1.

is a conserved quantity in this treatment. The conjugate variables describing electron cross-field drift are (A, Y). Hamiltonian equations for (5) are

$$\dot{s} = \frac{1}{m} p_{\parallel}, \qquad \dot{p}_{\parallel} = -\mu \frac{\partial \Omega_0}{\partial s}$$
$$\dot{A} = \mu \frac{e}{c} \frac{\partial \Omega_0}{\partial Y}, \qquad \dot{Y} = -\mu \frac{e}{c} \frac{\partial \Omega_0}{\partial A} \tag{6}$$

Figure 3a shows electron bounce motion for three α_{eq} values. There are typical electron oscillations between magnetic mirror points determined by the $h = \mu\Omega_0(s)$ condition. Figure 3b shows electron 3D trajectories in (s, A, Y) coordinate space for a dipolarizing flux bundle that has come to rest. Electrons oscillate fast along the magnetic field lines and drift around the magnetic field enhancement in the (A, Y) plane. This is typical of electron trapping by the magnetic field gradient drift, well described for electrons interacting with dipolarizing flux bundles (e.g., Gabrielse et al., 2017). Figure 3c shows the same 3D trajectories for a moving dipolarizing flux bundle. Electrons trapped around the bundle due to the cross-field drift are transported by the dipolarizing flux bundle toward the Earth (larger A). When electrons reach sufficiently large background magnetic field, they can escape from the bundle and start drifting along Y. This is the classical mechanism of electron transport by dipolarizing flux bundles from the magnetotail toward the Earth (Eshetu et al., 2019; Gabrielse et al., 2016, 2017; Sorathia et al., 2018).

Electron interactions with a moving dipolarizing flux bundle are accompanied by electron adiabatic heating due to magnetic field increase, given that μ is constant (Birn et al., 2014; Gabrielse et al., 2016). Figure 4 shows electron energy and equatorial pitch-angle α_{eq} evolution along the orbits of Figure 3, though shown here for longer time intervals. For electrons with α_{eq} close to 90°, the energy increases almost linearly with the magnetic field magnitude, as expected for betatron heating $h \sim B_{eq}$. Electrons with smaller pitch-angles spend more time

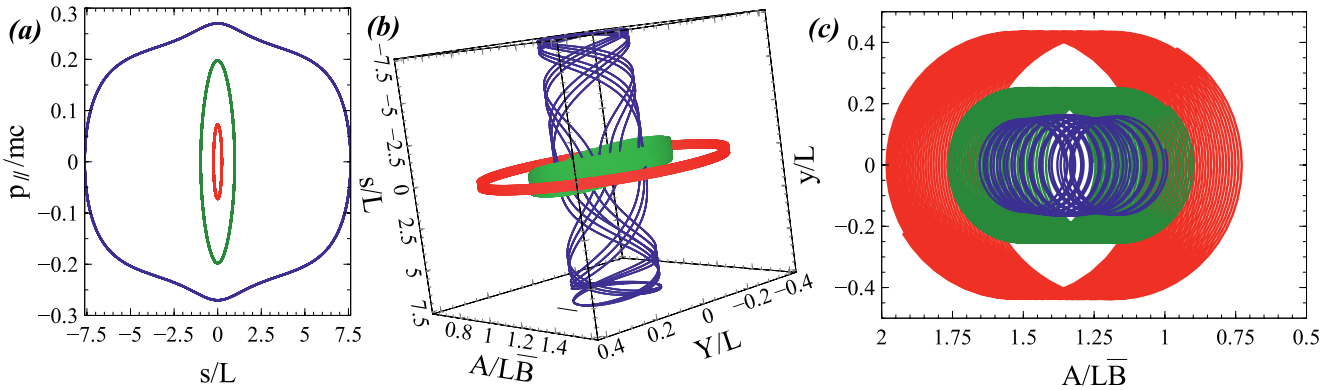

Figure 3. Three trajectories of electrons with 20 keV initial energy. Initial $A/L\bar{B} = 1$ (and $A_{0f}/L\bar{B} = 1$) and $Y/L = 0.4$, $\alpha_{eq} = 75°$ (red), $Y/L = 0.2$, $\alpha_{eq} = 45°$ (green), $Y/L = 0.05$, $\alpha_{eq} = 15°$ (blue). Other system parameters are the same as in Figure 1. Figures 1a and 1b shows trajectory projections in (s, $p_{\|}$) plane and in 3D space (A, Y, s) for a short time interval. (c) Shows trajectory projections in (A, Y) plane for a long time interval.

far from the equatorial plane in the weakly changing, off-equatorial field. Their parallel energy increases due to Fermi acceleration along a shrinking field line length, brought about by the motion of the dipolarizing flux bundle. If the field grows in intensity and shrinks in length as a dipole, the parallel energy increase occurs at a slower rate than the perpendicular energy increase (Tverskoy, 1969). Accordingly, the average electron energy

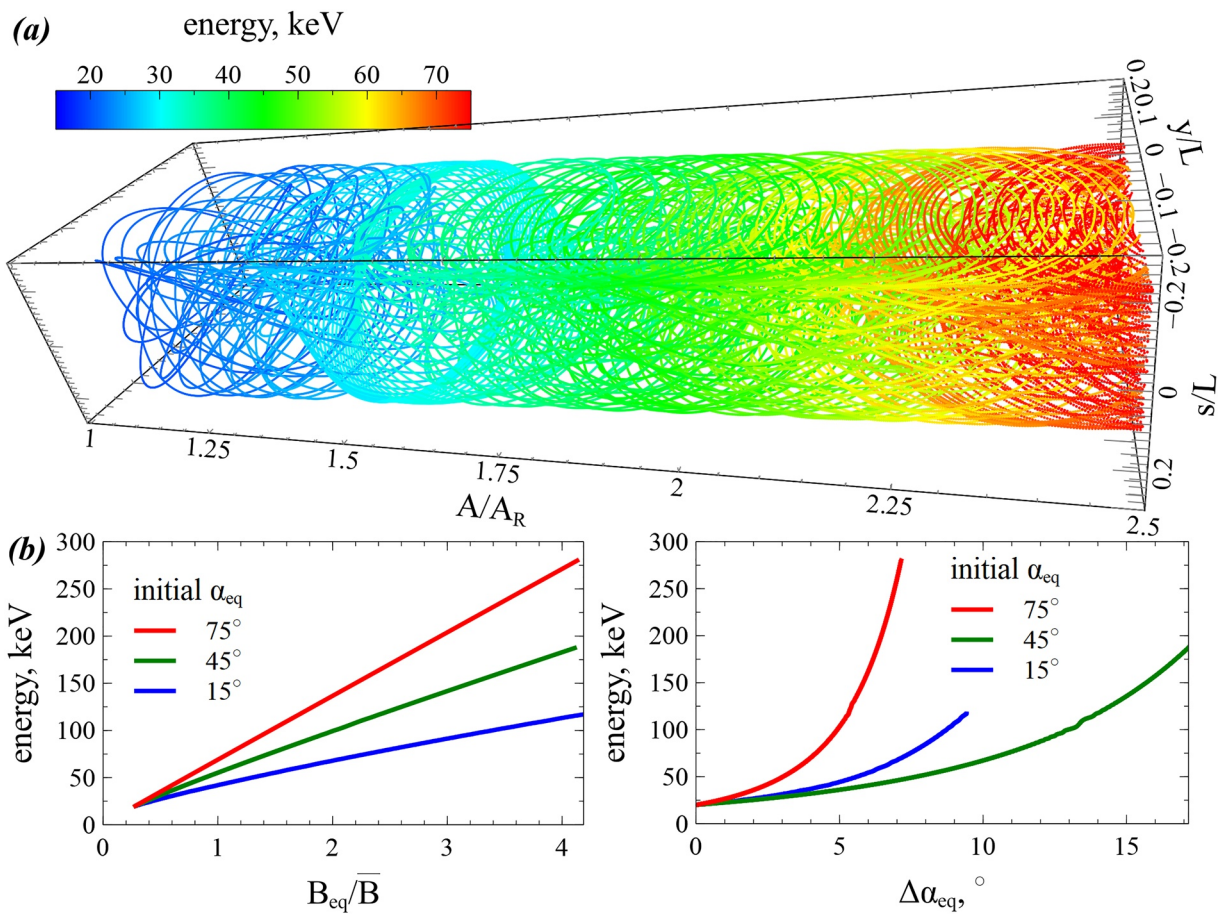

Figure 4. (a) Shows a fragment of (red) trajectory from Figure 3 in 3D space (A, Y, s), energies in colors. Bottom panels show energy and pitch-angle change of three trajectories of electrons with 20 keV initial energy. The equatorial field B_{eq} is B for $s = 0$. Initial $A/L\bar{B} = 1$ (and $A_{0f}/L\bar{B} = 1$) and $Y/L = 0.05$, whereas $\alpha_{eq} = 75°$ (red), $\alpha_{eq} = 45°$ (green), $\alpha_{eq} = 15°$ (blue). Other parameters are the same as in Figure 1.

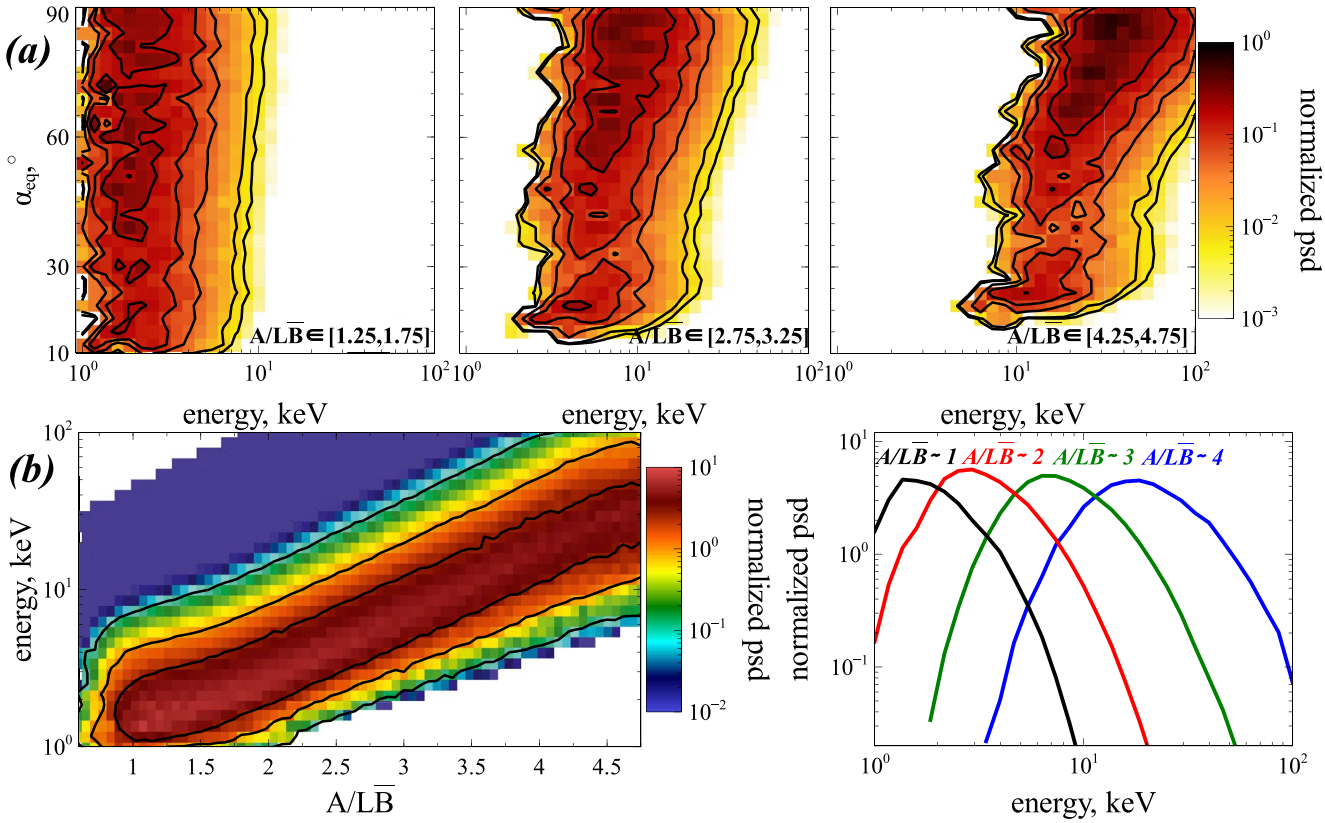

Figure 5. (a) Shows the normalized phase space density of electrons for three ranges of A/A_R (see Figure 1(f)). The initial electron phase space density is $\sim h^{1/2}\exp(-h/1\text{ keV})\sin^{1/4}\alpha_{eq}$. (b) Shows the electron distribution in (energy, $A/L\bar{B}$) space and several pitch-angle averaged electron spectra for different A/A_R. Model parameters are same as in Figure 1.

increases as $h \sim B^a$ with $a < 1$ (Artemyev et al., 2012; Lyons, 1984; Zelenyi et al., 2013). Such anisotropic heating can result in energetic electron distributions peaked around 90° (Fu et al., 2011, 2012; Motoba et al., 2020). However, local (energy and pitch-angle) electron distributions are often dominated by a fine interplay between dipolarizing flux bundle reconfiguration (Fu et al., 2013) and competing betatron and Fermi acceleration mechanisms (Birn et al., 2013; Fu et al., 2011; Runov et al., 2013). In our model, we use a stationary bundle configuration (without reconfiguration) and all the electron energization is due to the earthward motion of the dipolarizing flux bundle.

We numerically integrate 10^6 trajectories of electrons initially trapped (drifting around) within the dipolarizing flux bundle and calculate the evolution of their energy and pitch-angle distribution. Because the model background equatorial magnetic field $B = B(s, A, Y)$ (without the dipolarizing flux bundle) is a monotonic function of radial distance, it can be used as a proxy of that distance. We thus plot electron distributions for three different background magnetic field values represented by three different values of the vector potential in the three panels of Figure 5a. The figure shows that the energy of large pitch-angle electrons increases preferentially as the field increases (vector potential decreases), resulting in a *pancake* anisotropy ($\alpha_{eq} \sim 90°$) for tens to one hundred keV electrons. Such distributions are indeed observed around dipolarization fronts (Runov et al., 2013) and have been previously reproduced in numerical simulations (Birn et al., 2013, 2014). Figure 5b shows the evolution of the electron spectrum (pitch-angle averaged) during the earthward motion of the dipolarizing flux bundle. Adiabatic electron heating is clearly seen, with a self-similar evolution of the electron spectrum (in agreement with spacecraft observations of energetic electrons, see Fu et al., 2011; Runov et al., 2015).

The adiabatic heating accompanied by transverse anisotropy observed in the model is, in fact, typical of energetic electrons in Earth's magnetotail. This transverse anisotropy drives whistlers (Malykhin et al., 2021; Zhang

et al., 2019) often observed around dipolarizing flux bundles (Breuillard et al., 2016; Khotyaintsev et al., 2011; Le Contel et al., 2008; Zhang et al., 2018). Thus, in the next section we investigate electron resonant interaction with such waves over the time-scale of electron transport by a dipolarizing flux bundle.

3. Resonant Wave-Particle Interaction

We now revise the Hamiltonian Equation 5 by adding in Equation 7 a term describing the electron interaction with a field-aligned whistler wave of amplitude $\sim B_w$ and phase ϕ ($\partial\phi/\partial t = -\omega$ is the wave frequency and $\partial\phi/\partial s = k(s)$ is the wavenumber; see Appendix B and Vainchtein et al. (2018)).

$$H = \frac{1}{2m}p_{\parallel}^2 + \mu\Omega_0 + \sqrt{\frac{2\mu\Omega_0}{mc^2}}\frac{eB_w}{k}\sin(\phi+\psi) \tag{7}$$

The wave term also depends on the electron gyrophase, ψ. Thus the magnetic moment is not conserved in new Hamiltonian (7), because $\dot{\mu} = -\partial H/\partial\psi$. We introduce the quantity $\zeta = \phi + \psi$ with a time derivative:

$$\dot{\zeta} = k\frac{p_{\parallel}}{m} - \omega + \Omega_0 = \Omega_{eq}(Y,A)\cdot\left(\frac{kc}{\Omega_{eq}}\frac{p_{\parallel}}{mc} - \frac{\omega}{\Omega_{eq}} + f_b(s)\right) \tag{8}$$

where the wavenumber is given by the cold plasma dispersion relation (Stix, 1962):

$$kc/\Omega_{eq} = (\Omega_{pe}/\Omega_{eq})\cdot(\Omega_{eq}f_b(s)/\omega - 1)^{-1/2}$$

In Equation 8, $f_b(s)$ describes the background magnetic field intensity along magnetic field lines (see Figure 1e), whereas Ω_{eq} is a proxy of the magnetic field variation on the equatorial plane (Y, A) (see Figures 1f and 2d). Since whistlers are generated locally near the equator at all radial distances, the ω/Ω_{eq} distribution can be kept fixed independently of Y and A. The equatorial plasma density increases with A (as the radial distance decreases, see, e.g., Artemyev, Angelopoulos, et al., 2017) and we take Ω_{pe}/Ω_{eq} to be constant in order to simplify the evaluation of wave-particle resonant interactions. (In reality, this ratio will vary both with Y and A as the density and magnetic field vary with equatorial distance from a dipolarizing flux bundle, see e.g., Liu et al., 2013; Runov, Angelopoulos, Zhou, et al., 2011, so in future direct comparisons with observations wave-particle resonant effects should be evaluated separately for different (Y, A) locations.) For simplicity in our calculations we also assume an adiabatic equation of state for the flux tube plasma, implying a constant density along magnetic field lines, that is, Ω_{pe} is independent of s (this simplification may not be accurate in the near-Earth magnetotail where field-aligned gradients of plasma density are expected to be strong, see Artemyev, Zhang, et al., 2018).

Figure 6 shows several examples of electron trajectories, including both effects of adiabatic heating and nonlinear resonant interactions comprising phase bunching (evidenced in (a) as a gradual energy decrease due to many small $\Delta h_{scat} < 0$ energy changes in each interaction) and phase trapping (due to few large energy increases, $\Delta h_{trap} > 0$). As the electron bounce time is much faster than their adiabatic transport and associated heating, several incidents of wave trapping and scattering can occur around the equator before the electron energy can evolve adiabatically due to transport. Therefore, electron energy changes occur cyclically, each cycle comprising large energy increases due to trapping and gradual energy decreases due to bunching (see details in Artemyev, Neishtadt, et al., 2021). To mimic wave generation at the magnetic field minimum and propagation along magnetic field lines, we assume that wave amplitude B_w grows from zero at the equator to saturation at a peak value at some off-equatorial distance beyond which it stays constant (see the empirical models for the the inner magnetosphere, e.g., Agapitov et al., 2015, 2018). This distribution of wave power along magnetic field lines is such that trapping occurs for small energies and accelerates electrons, and then bunching can bring those electrons back from large energies to smaller energies where trapping becomes possible again (see details in, e.g., Artemyev, Vasiliev, et al., 2015; Vainchtein et al., 2018). Such large energy variations due to resonant wave-particle interactions can mask the much slower adiabatic heating on short timescales, but such heating should be distinguishable over the much longer, adiabatic transport timescales. The energy increase due to trapping is accompanied by a pitch-angle increase, whereas energy decrease due to bunching is accompanied by pitch-angle decrease. The latter moves electrons closer to the loss-cone. These rapid pitch-angle variations also affect the slower, adiabatic heating as

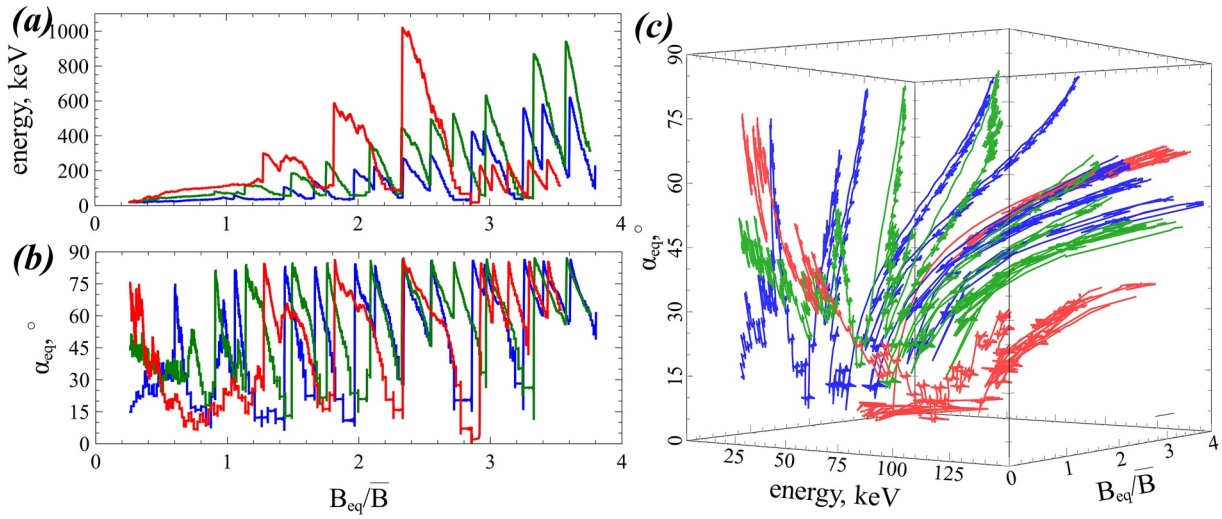

Figure 6. Three examples of electron trajectories from numerical integration of Hamiltonian equations for Hamiltonian (7). The background magnetic field parameters are the same as in Figure 1. The wave field amplitude is $0.02 \cdot B_{eq} \cdot f_w(s/L)$, where $L = 1R_E$ is the typical spatial scale of magnetic field inhomogeneity, $f_w = s/(s + L/4)$ for $s > 0$ and $f_w = 0$ for $s < 0$ (i.e., we consider a wave generated at the equator $s = 0$, propagating to $s > 0$ with an amplitude increase and saturation to peak value at around $L/4$ distance from the equator). Wave frequency is $0.35\Omega_{eq}$, and plasma frequency is $10\Omega_{eq}$. *Note.* (c) Shows 3D fragments of orbits from (a) and (b), that is, the energy range of (c) are limited to 150 keV for illustration purpose.

the latter depends on the μ value ($\partial H/\partial B \sim \mu$). In Figure 6 we consider only one wave propagating with $k > 0$ above the equator, and a single resonance per bounce period, to simplify test particle simulations. Appendix C generalizes this description to multiple resonances with more than one wave.

A numerical evaluation of the trajectories of electrons interacting with whistlers requires a sufficiently accurate tracing of the fast rotating wave phase and gyrophase. Therefore, for a large electron ensemble and multiple wave characteristics, such simulations cannot be performed within the test particle approach with present-day computers. Instead, we use the mapping technique initially proposed for the description of diffusive electron scattering (e.g., Chirikov, 1979; Vasilev et al., 1988) and generalized for nonlinear wave-particle interactions in Artemyev et al. (2020b). The approach is to consider electron resonant interactions as independent and instantaneous changes of the energy (μ and pitch-angle), that is, we describe electron motion with μ = const (using Hamiltonian (5)), and change μ after each half of the bounce period (e.g., at the equator) with a μ change (energy and pitch-angle changes) described by a probability distribution function. This function describes the probability of electron interaction with different waves from a wave distribution $\mathcal{P}(B_w, \omega)$ including the probability of electron to be phase trapped or bunched (see details in Appendix C and Artemyev et al. (2020b); Artemyev, Neishtadt, et al. (2021)). The inputs are the wave distribution $\mathcal{P}(B_w, \omega)$ and a model of $\Delta h_{scat,trap}$ changes. Appendix B gives $\Delta h_{scat,trap}$ evaluated for given characteristics of the background magnetic field Ω_0 and waves B_w, ω. Note that we normalize the wave frequency to the equatorial gyrofrequency, $\Omega_{eq} = \Omega_0|_{s=0}$.

Figure 7 shows several electron trajectories calculated for the wave amplitude and frequency probability distribution

$$\mathcal{P} \sim \exp\left(-(B_w - 200\text{pT})^2/150^2\text{pT}^2 - (\omega/\Omega_{eq} - 0.35)^2/0.225\right)$$

with $\langle B_w \rangle = 200$ pT and $\langle \omega \rangle = 0.35\Omega_{eq}$, same as used for the calculations in Figure 6. Electron trajectories obtained using this mapping technique reproduce the main features of the test-particle trajectories, but the numerical evaluation is much faster allowing us to trace a large ensemble of electrons even with limited computer resources. Then we will use a realistic $\mathcal{P}(B_w, \omega)$ distribution and a realistic initial electron distribution $F(h, \alpha_{eq})$. In the next section, we obtain such distributions from an example of spacecraft measurements in the magnetotail, and then examine the role played by whistlers in the evolution of the electron distribution as it interacts with the dipolarizing flux bundle.

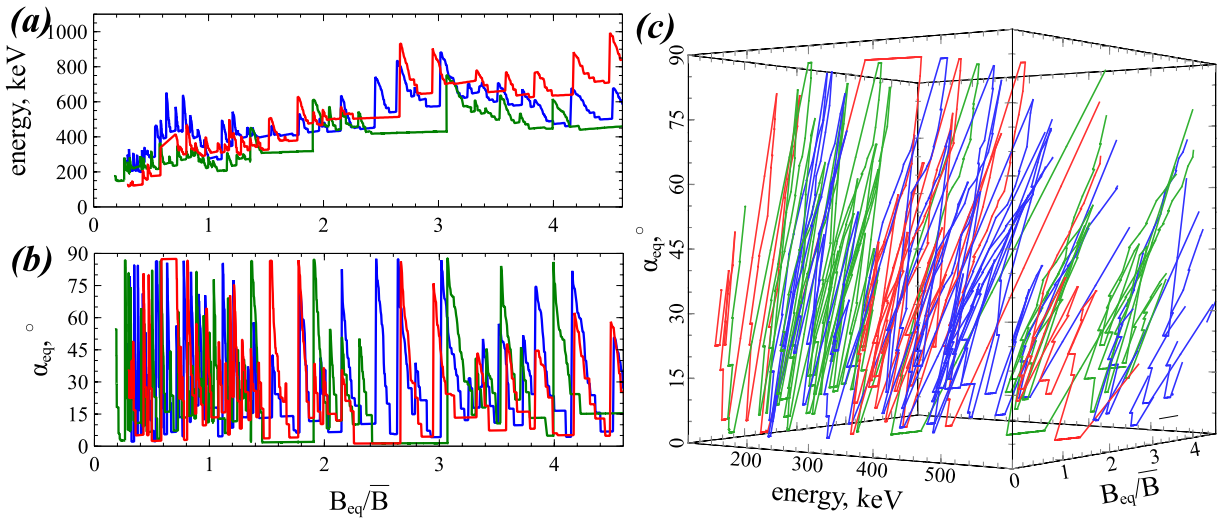

Figure 7. Three examples of electron trajectories from the numerical integration of Hamiltonian Equation 6 with the mapping technique, to evaluate electron resonant interactions with whistlers. The background magnetic field parameters are the same as in Figure 1. Wave amplitudes and frequencies are distributed with $\mathcal{P} \sim \exp\left(-(B_w - 200\text{pT})^2/150^2\text{pT}^2 - (\omega/\Omega_{eq} - 0.35)^2/0.225\right)$. Plasma frequency is $10\Omega_{eq}$, and $\Omega_{eq} = \Omega_0|_{s=0}$ is the equatorial gyrofrequency. *Note.* (c) Shows 3D fragments of orbits from (a) and (b), that is, the energy range of (c) are limited to 600 keV for illustration purpose.

4. Examples of Dipolarizing Flux Bundles

To use a realistic $\mathcal{P}(B_w, \omega)$ wave probability distribution, we examine one dipolarizing flux bundle event measured by THEMIS. We use magnetic field measurements by the fluxgate magnetometer (Auster et al., 2008) with 1/3 s resolution, thermal (<25 keV) ion and electron moments measured by the electrostatic analyzers (McFadden et al., 2008) with 3 s resolution, electron spectra (100 eV–100 keV) from combined measurements of the electrostatic analyzer and solid state telescope (Angelopoulos et al., 2008; Turner et al., 2012), and magnetic field fluctuations in the 10–4,000 Hz frequency range measured by the search-coil (Le Contel et al., 2008). We use both waveforms measured in the wave burst mode and wave spectra evaluated on board at 1s time resolution (Cully et al., 2008).

Figure 8 shows observations of the plasma injection, including increase of energetic electron fluxes and surrounding wave activity. THEMIS observed this injection well within the flow breaking region (Dubyagin et al., 2011; Nakamura et al., 2009), and there is no clear B_z enhancement (typical for dipolarizing flux bundle) and a quite weak earthward plasma flow (see Figure 8a). However THEMIS observed a clear energetic electron injection (see Figure 8b), which is typical signatures of dipolarizing flux bundles downtail (Nakamura et al., 2002, 2004; Runov et al., 2009). Therefore, we assume that THEMIS observed electrons transported by a dipolarizing flux bundle from the magnetotail. THEMIS observed this injection around the equatorial plane: $|B_x|$ is smaller than (or comparable to) B_z. The injection is also associated with a decrease in plasma density and a minimum of the local plasma frequency to gyrofrequency ratio (not shown). Based on these observations, for evaluation of wave-particle interactions we will use $\Omega_{pe}/\Omega_{ce} = 10$ at the equator and a constant Ω_{pe} along magnetic field lines (in agreement with the approximately constant density along magnetic field lines in magnetotail models; see, e.g., discussion in Artemyev & Zelenyi, 2013).

There is a clear enhancement of energetic electron fluxes (see Figures 8b and 8c), that is, the dipolarizing flux bundle transports and adiabatically heats electrons from the magnetotail (Birn et al., 2015; Gabrielse et al., 2016; Runov et al., 2015). The electron pitch-angle distribution (see Figure 8d) is dominated by cold field-aligned electrons (<1 keV; seen behind the injection front) and hot transversely anisotropic electrons (>5 keV; seen on THEMIS *A* and *E* behind the injection front). The transverse heating of hot electrons may be explained by adiabatic effects of electron transport into the spatially growing magnetic field (Birn et al., 2012; Fu et al., 2013; Gabrielse et al., 2014; Turner et al., 2016), whereas cold field-aligned beams are likely of ionospheric origin or result from electron field-aligned acceleration/scattering by kinetic Alfven waves (Artemyev, Rankin, & Blanco, 2015; Damiano et al., 2015) and/or electrostatic turbulence (Mozer et al., 2015; Shen et al., 2021; Vasko et al., 2017).

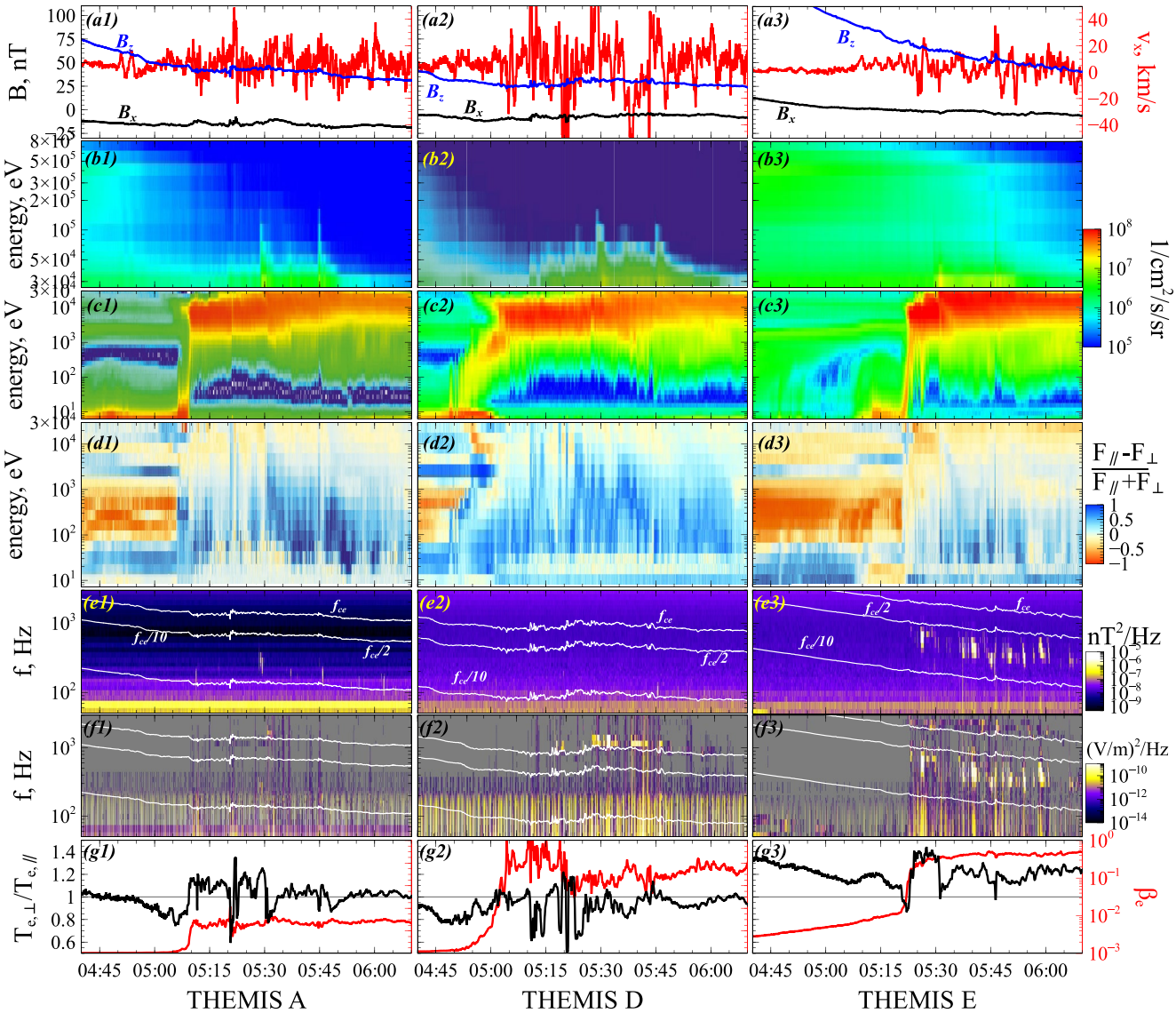

Figure 8. Overview of a plasma sheet injection observed by three THEMIS spacecraft on 4 July 2021: ThA data are on the left column with #1 panels, ThD data are on the center column with #2 panels, ThE data are on the right column with #3 panels. (a) Shows two magnetic field components (left axis) and ion flow v_x in red (right axis). (b) and (c) Shows electron energy flux from SST and ESA. (d) Shows anisotropy of electron flux in the ESA energy range. (e) and (f) Shows magnetic and electric field spectra and three characteristic frequencies depicted by white curves (f_{ce} is the local electron cyclotron frequency). (f) Showd the electron temperature anisotropy (left axis) and electron β_e, the ratio of electron to magnetic field pressure (right axis).

The description of the dynamics of this cold electron population would require to include field-aligned electric fields (see discussion in An et al., 2021; Génot et al., 2004; Shen et al., 2020), but this population is not considered in our study.

There are sporadic and transient bursts of whistlers around the dipolarizing flux bundles (see Figure 8e for THEMIS *E*). The wave spectrum $B_w^2(f)$ with $f = \omega/2\pi$ shows intense bursts around $f \in [0.1, 0.4]f_{ce}$ (with $f_{ce} = \Omega_0/2\pi$), in the typical frequency range of whistlers captured around dipolarizing flux bundles (Breuillard et al., 2016; Grigorenko et al., 2020; Le Contel et al., 2009; Zhang et al., 2018). Waves are mostly seen by THEMIS *E*, and less by THEMIS *A*, whereas THEMIS *D* observed only electron cyclotron harmonics (electric field bursts above f_{ce}). These differences in spacecraft observations can be explained by the differences of local electron anisotropic populations (see Figure 8d): THEMIS *E* and *A* observed transversely anisotropic hot electrons (>5 keV) that are the primary free-energy source for whistler waves (Kennel, 1966; Sagdeev &

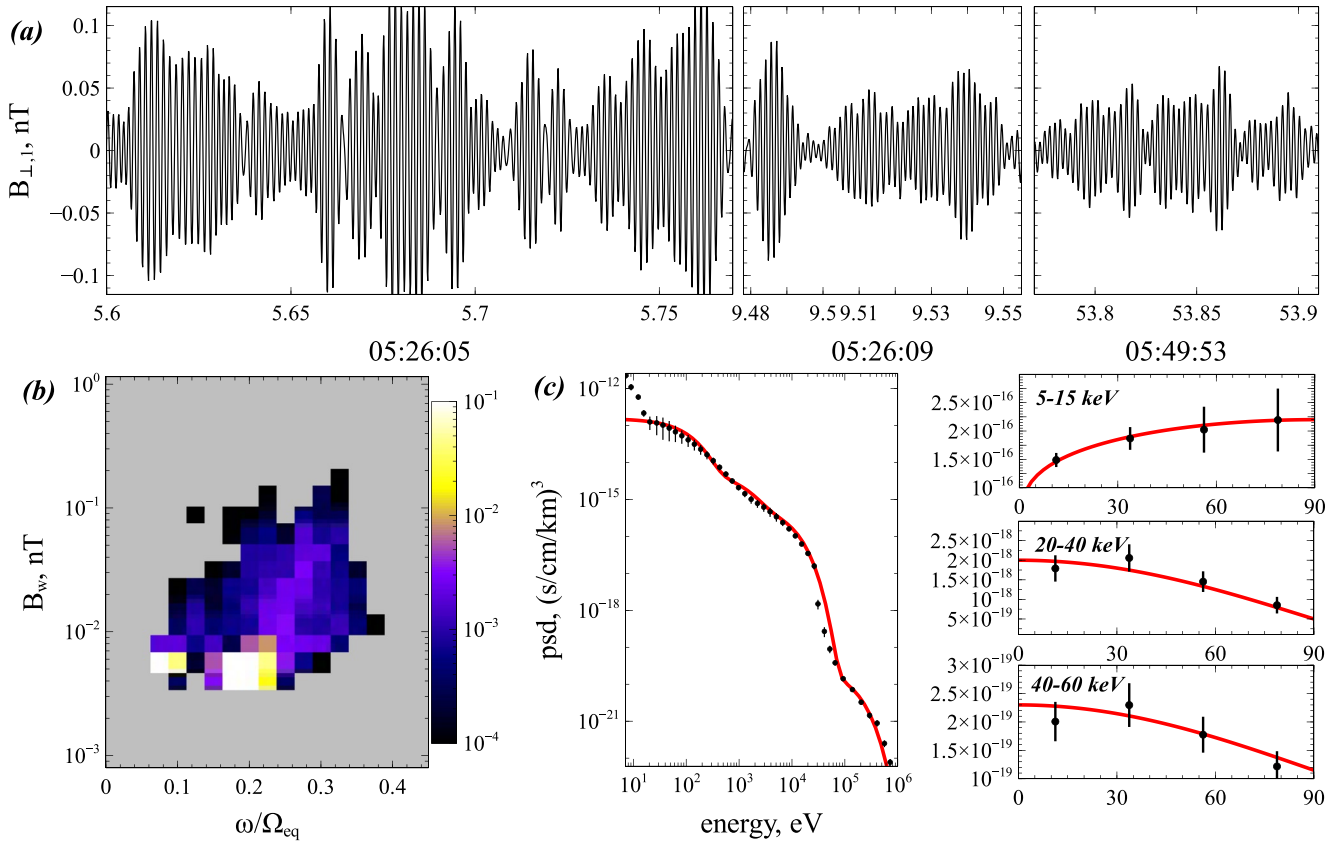

Figure 9. (a) Shows several examples of whistler wave packets observed by ThE (frequency range is between 300 Hz and 1 kHz). (b) Shows the distribution of whistler wave amplitude and frequency from *FFF* dataset with the power spectra integration within $[f_{ce}/10, f_{ce}/2]$ frequency range. (c) Shows measured electron energy spectrum and pitch-angle spectra (in black) for the interval 05:30–05:45, and results of our fitting procedure (in red).

Shafranov, 1961). Figure 8g show that electron temperature anisotropy and electron β are larger on THEMIS E, leading to a higher amount of whistlers there.

For each 1s spectrum we calculate the RMS time-averaged wave amplitude $B_w = \left(\int_{f_{ce}/10}^{f_{ce}/2} \mathcal{B}_w^2 df\right)^{1/2}$ and mean wave frequency $f_m = \int_{f_{ce}/10}^{f_{ce}/2} \mathcal{B}_w^2 f df / B_w^2$. These wave characteristics are input parameters for the mapping technique. B_w^2 is the time-averaged wave intensity calculated from wave spectra. The amplitude of individual wave-packets can be significantly larger than B_w. This difference is not important for the quasi-linear diffusion describing wave-particle resonant interaction by diffusion rates that depend only on the time-averaged B_w (Lyons & Williams, 1984; Schulz & Lanzerotti, 1974). For nonlinear resonant interactions, however, the electron dynamics are determined by peak wave amplitudes and the occurrence rate of intense waves. Therefore, we need to recalculate the B_w distribution derived from the wave spectra integration to estimate the actual occurrence rate of intense waves. This is done by using simultaneous measurements of whistler wave packets (see Figure 9a). Typical wave packet amplitudes during this event are ~100 pT, that is, a factor $K \approx 20$ larger than the average $B_w \sim 5$ pT and a factor $K \approx 5$ larger than the level $B_w \sim 20$ pT of the most intense wave population (see the $\mathcal{P}(B_w, f/f_{ce})$ distribution in Figure 9b). Accordingly, we multiply the time-averaged B_w by $K = 5$. To keep the same time-averaged wave intensity B_w^2 we assume that such intense wave packets are observed only a fraction $1/K^2$ of the time, whereas during the rest $1 - 1/K^2$ of the time there are no whistlers. This may be simplistic but nonetheless captures the essential features of the wave packet for the purpose of nonlinear interactions. Thus, during each half of the bounce period, there is a probability $1/K^2$ that an electron resonates with one of the waves from the $\mathcal{P}$ distribution, and a probability $1 - 1/K^2$ that there is no resonant interaction and thus electron characteristics remain unchanged.

To set the initial electron distribution function $F = F_0(h)\sin^C\alpha_{eq}$, we determine C, $F_0(h)$ by fitting the measured electron fluxes. Figure 9c shows such fits of the pitch-angle averaged phase space density which provide fitting parameters $F_0 = \sum_{k=1,2} A_k \cdot \exp(-h/h_k)$ with $A_1 \approx 1.5 \cdot 10^{-13}$, $A_2 \approx 5 \cdot 10^{-15}$, $h_1 \approx 0.1$ keV, and $h_2 \approx 1$ keV. Note that we only fit the low-energy part of the electron distribution and do not include the high-energy electron population into the initial distribution for the simulation, because we assume that this population is formed during adiabatic heating and, thus, should be reproduced (at least partially) by our model. Figure 9c also shows fits of the pitch-angle distributions for several energy ranges: thermal electrons are transversely anisotropic, and high energy electrons are almost isotropic or weakly parallel anisotropic. Thus, we use $C \approx 1/4$ for $h < 50$ keV. Note that THEMIS is located in the injection region, whereas the initial cold F distribution should be taken further down the magnetotail where electron density is much smaller. Thus, we keep the energy spectrum of cold electrons, but normalize the electron density (the integral of F) at the starting point of the particle trajectory (where $B_{eq}/\bar{B} \approx 0.2$) such that it attains the measured density at the observation region (where for our model we have $B_{eq}/\bar{B} \approx 6$). For such a normalization, we use a factor $\sim B_{eq}^{2/3}$ that reflects the typical variation of the electron density along the magnetotail (Tsyganenko & Mukai, 2003; Wang et al., 2009).

The magnetic field model includes a term $A - cE_f t$ that determines the time-scale (or electric field magnitude) of dipolarizing flux bundle motion. This time-scale can be estimated based on the measured front speed v_f together with a magnetic field model. The front velocity can be as large as 500−1,000 km/s in the middle tail (Hwang et al., 2011; Runov, Angelopoulos, Sitnov, et al., 2011; Runov et al., 2009), but it decreases to tens of km/s around the plasma flow braking region (Dubyagin et al., 2011; Liu et al., 2014, 2016). Thus, we use $v_f \approx 200$ km/s, which is typical, and for simplicity's sake do not include effects of flow braking (such braking can be incorporated into the model, if needed, as a variable profile of $v_f(x)$, see Artemyev, 2014; Gabrielse et al., 2017). The magnetic field model assumes that the equatorial non-perturbed (without dipolarizing flux bundle) magnetic field magnitude changes from 1 to 100 nT for $A/L\bar{B} \in [0.5, 5]$ (see Figure 1f for $\bar{B} = 30$nT). This range of magnetic field variation generally corresponds to the range of radial distances $[26, 6]R_E$. Therefore, the dipolarizing flux bundle will travel this distance in $\Delta t = 24R_E/v_f \approx 600$ s, and have an electric field $E_f = \Delta A/\Delta t c = 4.5 \cdot \bar{B}L/\Delta t c \approx 2$mV/m (which is typical of the average electric field on dipolarization fronts, see Runov, Angelopoulos, Zhou, et al. (2011)). Since such simplified estimates do not take into account the front braking (Liu et al., 2014, 2016), we likely underestimate the travel time and the number of resonant wave-particle interactions. We should also note that electrons are not (all) transported by the dipolarizing flux bundle to the region of >100 nT background field, but rather (most) manage to escape from the bundle when the background field reaches the bundle field intensity the electrons are trapped in (see Gabrielse et al., 2016, 2017).

Figures 10a1–10c1 shows a set of electron distribution functions $F(h, \alpha_{eq})$ obtained from numerical integration of 10^6 electron orbits, without effects of resonant interactions with whistlers. The electron distributions are shown at different magnitudes of the equatorial magnetic field, a proxy of the radial distance. There is clear adiabatic heating and the formation of a transverse anisotropy, as previously seen in Figure 5a. These distributions are computed after spatial averaging around the dipolarizing flux bundle ($A/\bar{B}L \in \left(cE_f t/\bar{B}L\right) \cdot [0.5, 1.5]$, $Y \in [-1, 1]$). Next, Figures 10a2–10c2 shows electron distributions at the same radial distances as Figures 10a1–10c1 above them, but now with the effects of whistlers included. Electron resonant interactions with whistlers mix electrons in (energy and pitch-angle) space along the resonance curves. This results in energetic electron deceleration due to phase bunching by whistlers and a reduction of electron pitch-angle perpendicular anisotropy at such energies. Electron transport to smaller pitch-angles by phase bunching also creates a secondary energetic population at low pitch-angles, $\alpha_{eq} < 30°$. This population is less energized than the main, adiabatically heated population with $\alpha_{eq} > 60°$, because of the aforementioned phase bunching and also because adiabatic heating is much less efficient for low pitch-angle electrons. The particular shape of $F(h, \alpha_{eq})$ depends on the current sheet configuration (which ultimately dictates the efficiency of adiabatic heating for different α_{eq}, see, e.g., Artemyev et al., 2012) and on the spatial distribution of whistler wave intensity along magnetic field lines ($B_w(s)$ determines the energy range of cyclotron resonant electrons for different α_{eq} (Agapitov et al., 2018; Mourenas et al., 2014) and the efficiency of phase trapping (Artemyev, Vasiliev, et al., 2015; Vainchtein et al., 2018). Therefore, additional simulations with different current sheet configurations, $f_b(s)$, and wave amplitude profiles $B_w(s)$ would be needed to investigate the full range of possible $F(h, \alpha_{eq})$ shapes.

Figure 11 compares electron energy spectra (pitch-angle averaged) at several radial distances (denoted by their equatorial magnetic field values) and three interaction models: adiabatic heating only (top row), and adiabatic

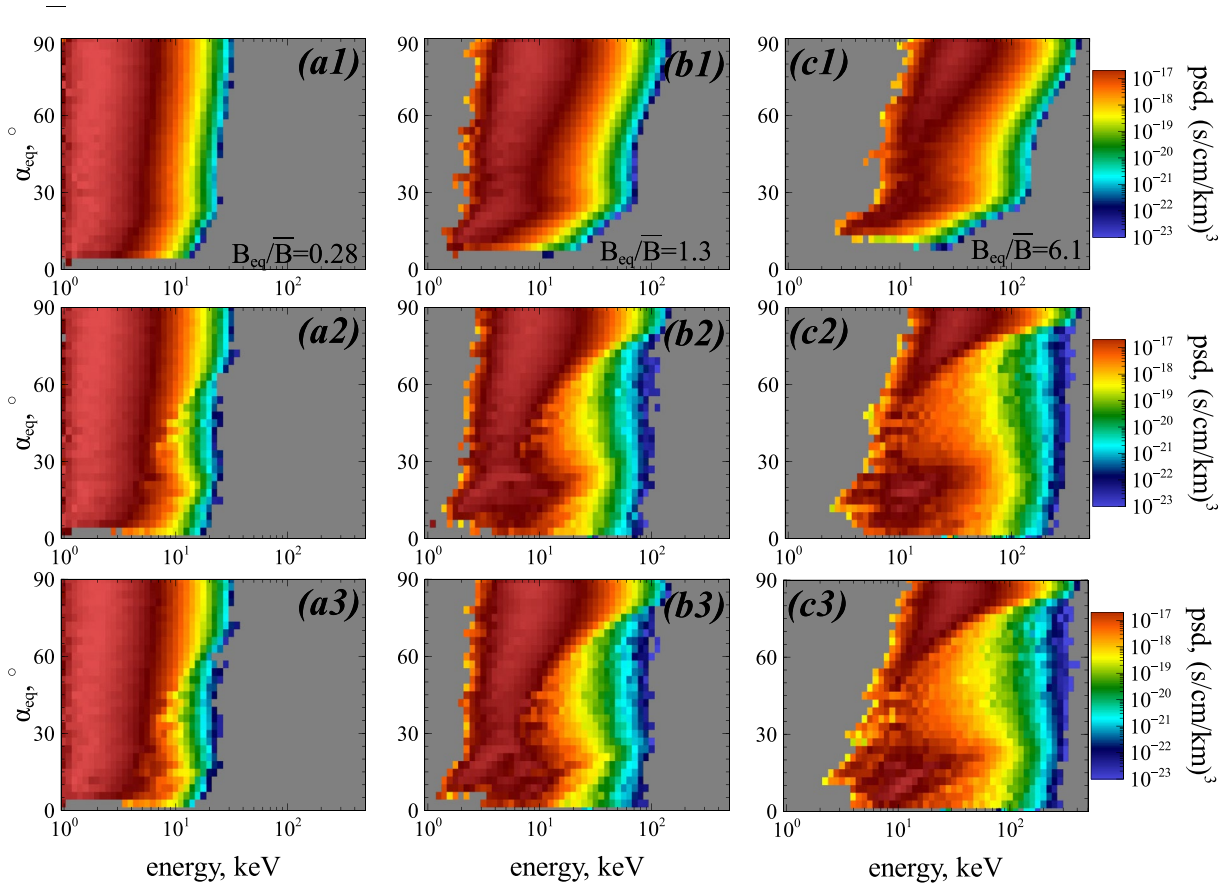

Figure 10. Electron (energy and pitch-angle) distributions for different B_{eq} values (shown as inserts on the top row panels). (a1–c1) show results of electron tracing without wave-particle interaction effects. Rows show results of electron tracing after including effects of electron scattering by whistlers for $K = 5$ in (a2–c2), and $K = 10$ in (a3–c3; see text for details). Tracing was started at $B_{eq}/\bar{B} \approx 0.2$. The initial distribution function was taken from a fit to the electron spectrum of Figure 9c below <5 keV after maintaining the spectrum but rescaling the electron density (zero moment of the electron distribution function) to correspond to $B_{eq}/\bar{B} \approx 0.2$, down from $B_{eq}/\bar{B} \approx 6$ at its measurement location on THEMIS, using a multiplication factor $\sim B_{eq}^{2/3}$ that mimics the observed variation of the electron density along the magnetotail (Tsyganenko & Mukai, 2003; Wang et al., 2009).

heating plus wave-particle resonant interactions for $K = 5$ (middle row) and for $K = 10$ (bottom row). (We use a higher K to check if this parameter affects significantly simulation results.) Evidently, these pitch-angle averaged energy spectra are not significantly influenced by electron scattering by whistlers, that is, such scattering mostly changes the electron pitch-angle distribution, but not the omni-directional energy spectrum. Interestingly, results for $K = 5$ and 10 are very close. This indicates that increasing the wave intensity and decreasing of probability of electron nonlinear resonant interaction with waves does not change the simulation results significantly, as long as there is a sufficiently large number of resonances for each electron in the tracing ensemble.

Electron scattering by whistlers may significantly decrease electron pitch-angles and move particles to the loss-cone. An accurate estimate of the loss-cone size for the near-Earth magnetotail is almost impossible, because empirical magnetic field models (Andreeva & Tsyganenko, 2019; Tsyganenko, 1995; Tsyganenko & Sitnov, 2007), with only few exceptions (Sitnov et al., 2021; Stephens et al., 2019; Tsyganenko et al., 2021), do not include the effects of dipolarization associated with plasma injection and strong variations of the equatorial magnetic field (such variations may significantly change the loss-cone size and precipitating electron fluxes, see, e.g., Eshetu et al., 2018). Typical loss-cone angle α_{LC} estimates give $\leq 2°$ in the magnetotail (see Figure 3d in Zhang et al., 2015), and this value can be larger closer to the Earth. For a simulation of precipitating electron fluxes, we use $\alpha_{LC} = 3°$. This value could overestimate the precipitating flux magnitude, but there is almost no energy change due to the wave-particle resonant interaction at pitch-angles <3°. Therefore, the energy spectrum of precipitating electrons derived from our simulation should reproduce the expected spectrum of electrons

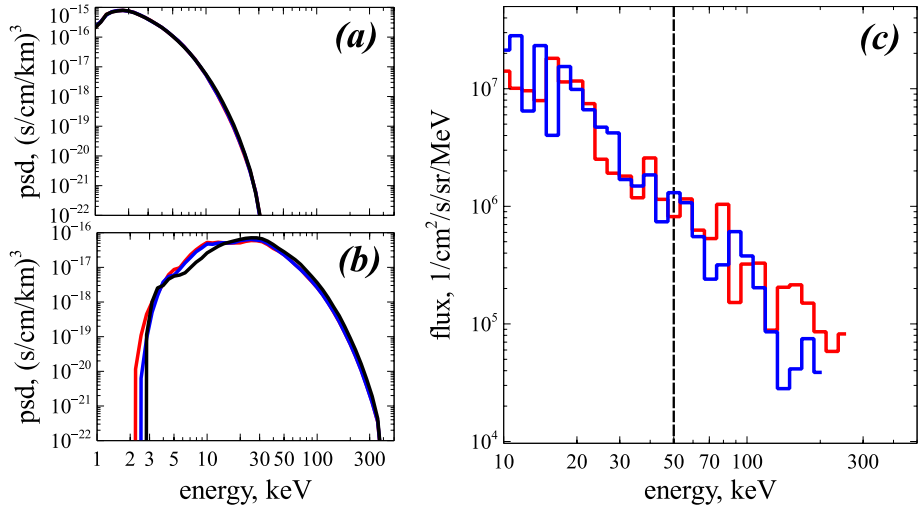

Figure 11. Pitch-angle-averaged electron spectra from Figure 10 for $B_{eq}/\tilde{B} \approx 2.8$ (a) and $B_{eq}/\tilde{B} \approx 6.1$ (b). In both figures, results without wave-particle interactions are shown in black, and with wave-particle interactions with $K = 5$ in blue, and with $K = 10$ in red. (c) Shows fluxes of precipitating electrons at $B_{eq}/\tilde{B} \approx 6.1$ for $K = 5$ (blue) and $K = 10$ (red). Vertical dashed line shows the starting energy of ELFIN measurements.

precipitating from the dipolarizing flux bundle region. To check this, we compare model results with observations from the low-altitude, polar-orbiting CubeSats ELFIN (Angelopoulos et al., 2020) that provide conjugate measurements for the event in Figure 8 (see Figure 12g for details of ELFIN and THEMIS orbits). Energetic particle detectors on board ELFIN measure electron pitch-angle and energy distributions, and thus allow us to investigate electron fluxes within the loss-cone j_{loss} as well as trapped fluxes j_{trap} (see details in, e.g., Artemyev, Demekhov, et al., 2021; Mourenas et al., 2021). We use 1.5 s (half-spin) time resolution ELFIN measurements, which provides full pitch-angle resolution. Figure 12 shows an overview of ELFIN A and ELFIN B trapped and precipitating fluxes for two times: First, ELFIN A crosses the L-shell region of THEMIS observations of plasma injection around the injection time (see Figure 12g denoting the conjunction times). Then, an hour later, ELFIN B visited the same L-shell range. (Note that L-shell values derived for projections of the low-altitude spacecraft are based on the empirical magnetic field model, which does not account for the magnetic field reconfiguration during the plasma injection, i.e., there is some uncertainty in ELFIN projections to the magnetotail.) Figures 12a and 12b shows j_{trap} distributions (from left to right, spacecraft move from larger to smaller L). Recurrent patterns of strong j_{trap} increase at the inner edge of the plasma sheet (05:39:00–05:39:45 for ELFIN A; 06:44:00–06:44:30 for ELFIN B). This flux increase is also associated with a high ratio $j_{loss}/j_{trap} \sim 1$ showing strong energy dispersion: larger energies with $j_{loss}/j_{trap} \sim 1$ are closer to the Earth (see Figures 12c and 12d). This pattern most likely corresponds to the electron isotropic boundary (Imhof et al., 1979; Sergeev et al., 2012; Yahnin et al., 1997), that is, energetic electron scattering in the current sheet due to the magnetic field line curvature (Birmingham, 1984; Büchner & Zelenyi, 1989; Lukin, Artemyev, Petrukovich, & Zhang, 2021; Young et al., 2002). The curvature scattering efficiency depends on energy and the equatorial magnetic field curvature radius and intensity. These dependencies are responsible for the observed energy dispersion (Dubyagin et al., 2021; Sergeev et al., 2018). Closer to the Earth, both ELFINs show a secondary burst of $j_{loss}/j_{trap} \sim 1$ and an increase of j_{trap} (around 05:39:55 for ELFIN A and 06:44:50 for ELFIN B), and this second precipitation pattern is not due to electron curvature scattering, because energies of precipitating electrons are lower than energies of the pattern associated with the isotropic boundary observed farther away from the Earth. For ELFIN A this second precipitation pattern is observed around its conjunction to the equatorial injection region observed by THEMIS. We thus attribute this pattern to electron scattering from the injection region (see Figures 12g). Figure 12e shows spectra of precipitating electrons. Their average spectral shape is similar to the precipitating electron fluxes derived from the simulation driven by THEMIS equatorial measurements of electron fluxes and whistlers (compare red and gray curves; see also Figure 11c). Therefore, our simulation confirms the importance of electron scattering by whistlers for electron losses (Ni et al., 2016; Nishimura et al., 2020) and the contribution of the energy input (Khazanov et al., 2018; Ni, Thorne, Meredith, et al., 2011) to the ionosphere by the injections.

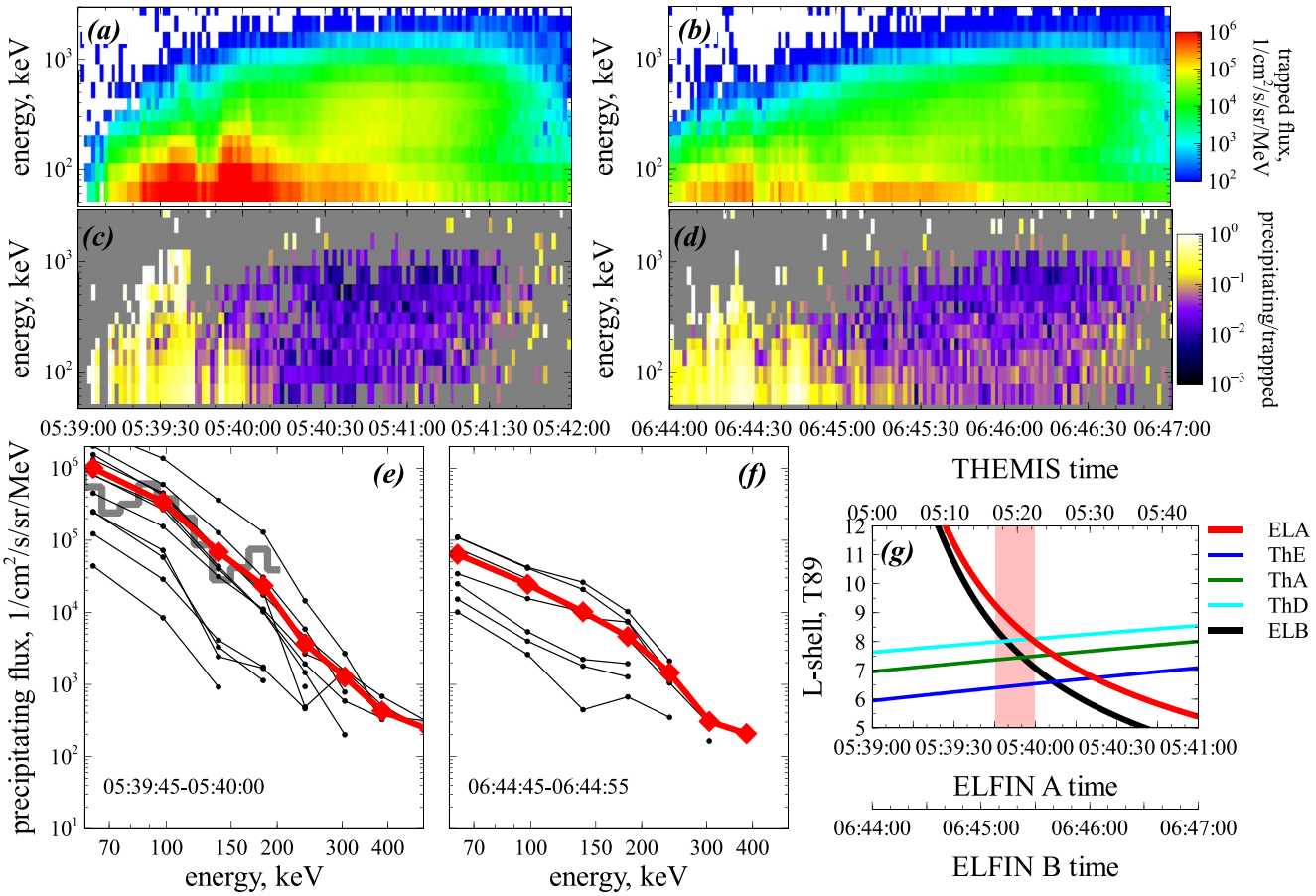

Figure 12. Overview of ELFIN A and B observations during the THEMIS injection event of Figure 9. (a) and (b) Show electron trapped fluxes (outside of the loss-cone) measured by ELFIN A during injection and ELFIN B 1 hr after injection, respectively. (c) and (d) Shows the ratio of precipitating to trapped electron fluxes. (e) and (f) Show energy spectra from ELFIN A and ELFIN B for two time intervals (listed within the panels) associated with enhanced electron precipitations. The gray curve in (e) shows the model result from Figure 11c. (g) Shows *L*-shell profiles of three THEMIS and two ELFIN satellites determined from the (Tsyganenko, 1989) model.

THEMIS observations show that the plasma flow associated with the injection in Figure 9 is almost completely suppressed, or the flow nearly completely brakes (as expected for plasma injections in the near-Earth region, see Dubyagin et al., 2011; Liu et al., 2014; Runov et al., 2015). Such stopped flux bundles containing trapped energetic electrons and whistlers can survive for a long time and form the so-called *pile-up* region in the near-Earth magnetotail (see Gabrielse et al., 2019 and reference therein). This region is continuously supplied new flux and associated particle fluxes (which appear as new injections), and gradually expands downtail (see discussion in Baumjohann, 2002). This may explain why ELFIN B still observed an enhanced j_{trap} and j_{trap}/j_{loss} earthward of the isotropic boundary as much as 1 hr after ELFIN A observations.

5. Discussion

In this study, we examined the effect of electron resonant interactions with whistlers around a dipolarizing flux bundle. Our approach combines the canonical guiding center theory and the mapping technique, allowing us to trace electrons in a magnetotail magnetic field configuration. There are, however, two important phenomena that we did not take into account. The first is electron curvature scattering in the magnetotail current sheet (Birmingham, 1984; Büchner & Zelenyi, 1989). This curvature scattering should destroy the conservation of μ, which is only an approximate integral of motion (Chirikov, 1979; Cohen et al., 1978; Howard, 1971; Neishtadt, 1984). Each electron crossing of the equatorial plane is associated with a jump $\Delta\mu \sim \exp(-1/\kappa^2)$ (Neishtadt, 2000; Slutskin, 1964; Su, 2012); here $\kappa^2 \ll 1$ is the ratio of the election gyroradius to the magnetic field line curvature radius. This μ variation does not change electron energy, but provides electron isotropization that

may be as effective as scattering by whistlers (Artemyev et al., 2013). Such curvature scattering is well modeled in test particle simulations of electron interaction with dipolarizing flux bundles (Eshetu et al., 2018; Sorathia et al., 2018), but it is omitted in our model of guiding center (μ = const) motion. The mapping technique, however, can include this effect of scattering by the magnetic field line curvature in the same way as scattering by whistlers. There are analytical models of electron μ jumps due to the curvature scattering (Anderson et al., 1997; Delcourt et al., 1994, 1995; Shustov et al., 2015; Young et al., 2008), and these models provide the magnitude of $\Delta\mu$ as a function of α_{eq} and κ. Thus, under an assumption of electron diffusion (zero mean $\Delta\mu$), in the future we can include the $\Delta\alpha_{eq}$ changes due to the curvature scattering given our magnetic model's $\kappa(A)$ profile.

The second important phenomenon we have not included is the electron feedback to the whistler wave intensity. Currents of phase trapped and phase bunched electrons change the whistler wave amplitude and frequency (Demekhov, 2011; Nunn, 1974; Nunn et al., 2009; Omura et al., 2007; Shklyar & Matsumoto, 2009), and thus wave intensity should depend on the local electron pitch-angle/energy distribution (see reviews by Omura, 2021; Tao et al., 2020). The most advanced and detailed models of such relationship either use particle-in-cell simulations (Katoh & Omura, 2007, 2016; Tao et al., 2017, 2021) or operate with joint Hamiltonians describing both electron and wave ensembles, including wave-particle energy exchange (Crabtree et al., 2017; Krafft & Volokitin, 2018). However, such a self-consistent approach of wave-particle interaction is computationally quite expensive. A simplified approach includes only the linear Landau damping of waves by suprathermal electrons (Bell et al., 2002; Bortnik et al., 2007; Chen et al., 2013; Katoh, 2014; Watt et al., 2013) or nonlinear wave damping/growth rates that are calculated for a given electron distribution and describe wave intensity variation along the wave ray path (Omura et al., 2013; Shklyar, 2011, 2017). But this alternative approach requires the consideration of 2D/3D wave motion with the wave ray divergence effect (Breuillard et al., 2012, 2013; Chen et al., 2013; Katoh, 2014). Furthermore, theoretical investigations would be needed to determine the best way for including electron feedback to the whistler wave ensemble into the proposed mapping technique.

As we aim to describe nonlinear effects of electron resonant interactions with whistlers, we did not include the effects of diffusion into the mapping. This excludes all low-intensity waves from the consideration. Electron diffusion by whistlers around the plasma injection region can be quite effective (Khotyaintsev et al., 2011; Ni, Thorne, Shprits, et al., 2011; Panov et al., 2013) and may exceed the strong diffusion limit ($j_{loss}/j_{trap} \sim 1$) in the ~1–10 keV energy range (Ghaffari et al., 2021). Thus, this diffusion may also contribute to electron scattering and losses. For the proposed mapping technique, there are two possible generalizations allowing us to include electron diffusion by low amplitude whistlers. First, the electron phase space trajectory equations can be supplemented by stochastic differential terms (Lukin, Artemyev, & Petrukovich, 2021; Tao et al., 2008) modeling the random electron pitch-angle/energy changes due to scattering by waves. Second, the scattering can be added directly into the map (see, e.g., the description of diffusion by the Chirikov map; Chirikov, 1979; Lichtenberg & Lieberman, 1983) and more sophisticated maps (Benkadda et al., 1996; Khazanov et al., 2014)). Both approaches rely on diffusion coefficients that can be derived in the quasi-linear approach for low-intensity waves (Ni et al., 2016) and directly from the analysis of electron trajectories for high-intensity waves (Albert, 2010; Artemyev et al., 2014; Karpman & Shkliar, 1977). Note that the natural inhomogeneity of the background magnetic field results in a stochastization of electron resonant interactions and allows an evaluation of the diffusion coefficients even for monochromatic whistlers (Albert, 2001, 2010; Solovev & Shkliar, 1986).

6. Conclusions

We proposed and tested a new approach for evaluating electron phase space dynamical evolution in response to both adiabatic heating due to transport across magnetic field gradient and wave-particle interactions. The approach combines the canonical guiding center model of electron adiabatic dynamics and the mapping technique for modeling electron resonances with whistlers. Using this approach we investigated the role of whistlers in scattering and acceleration of electrons interacting with a dipolarizing flux bundle in the Earth's magnetotail. We found that:

1. Electron scattering by whistlers around a dipolarizing flux bundle does not affect the electron omni-directional (pitch-angle averaged) energy distribution much. However, such scattering does change the electron pitch-angle distribution by reducing the perpendicular fluxes and enhancing the low pitch-angle fluxes of energetic electrons. This results in an isotropization that influences the evolution of electron adiabatic heating. In previous test-particle simulations, similar isotropization was achieved by energetic electron scattering due

to magnetic field line curvature (Birn et al., 2013; Eshetu et al., 2018). The relative contributions of curvature scattering and wave-driven scattering needs to be investigated in future studies

2. Electron scattering by whistlers (mostly from phase bunching) drives energetic electron precipitation from the injection region. Simulation results show significant precipitating fluxes over a wide energy range including 10 keV electrons, which ought to be contributing to the diffusive aurora (see Ni et al., 2016; Nishimura et al., 2020), and ~100 keV electrons, which ought to be detectable as riometer signatures of plasma injections (see Gabrielse et al., 2019; Spanswick et al., 2007). Therefore, electron scattering by whistlers from the plasma injection region can contribute significantly to the ground-based observations of such injections

Appendix A: Guiding Center Hamiltonian

We start with the Hamiltonian of a non-relativistic electron moving in the electromagnetic fields that can be described by the vector potential $\mathbf{A} = A(x, y, z, t)\mathbf{e}_y$:

$$H = \frac{1}{2m}\left(\mathbf{p} - \frac{e}{c}\mathbf{A}\right)^2 \tag{A1}$$

where $\mathbf{p} = (p_x, p_y, p_z)$ is the momentum conjugate to $\mathbf{r} = (x, y, z)$. The equations of motion for this Hamiltonian are

$$\begin{aligned} \dot{\mathbf{r}} &= \frac{1}{m}\left(\mathbf{p} - \frac{e}{c}\mathbf{A}\right) = \mathbf{v} \\ m\dot{\mathbf{v}} &= \dot{\mathbf{p}} - \frac{e}{c}\frac{\partial \mathbf{A}}{\partial t} = e\mathbf{E} + \frac{e}{c}\left[\mathbf{v}\times\mathbf{B}\right] \end{aligned} \tag{A2}$$

where $\mathbf{E} = -c^{-1}\partial\mathbf{A}/\partial t$ and $\mathbf{B} = \nabla\times\mathbf{A}$. The system of Equation A2 can be written as Hamiltonian equations for ($\mathbf{r}$, $\mathbf{v}$) if we introduce time as a new variable ϑ (such that $\dot{\vartheta} = 1$) and will use the non-degenerate 2-form

$$\Theta_\vartheta = m d\mathbf{v}\wedge d\mathbf{r} + dP_\vartheta \wedge d\vartheta - \frac{e}{c}\sum_{i<j}\Gamma_{ij} dr_i \wedge dr_j - e\mathbf{E}d\vartheta\wedge d\mathbf{r} \tag{A3}$$

where P_ϑ is the momentum conjugate to ϑ, $(r_1, r_2, r_3) = (x, y, z)$, $\Gamma_{12} = -B_z$, $\Gamma_{13} = B_y$, $\Gamma_{23} = -B_x$. Symbol $\wedge$ in Equation A3 means the exterior product operator (Arnold, 1989; Arnold et al., 2006) with the following properties: the exterior product of two vectors $\mathbf{a}_1$ and $\mathbf{a}_2$, $\mathbf{a}_1\wedge\mathbf{a}_2$ (called bivector) has the magnitude equal to the area of the parallelogram with sides corresponding to vectors $\mathbf{a}_1$ and $\mathbf{a}_2$; this operation is antisymmetric, $\mathbf{a}_1\wedge\mathbf{a}_2 = -\mathbf{a}_2\wedge\mathbf{a}_1$, and $\mathbf{a}_1\wedge\mathbf{a}_1 = 0$.

Implying that Θ_ϑ is closed ($d\Theta_\vartheta = 0$) and using it as a symplectic structure for Hamiltonian ($dH = \Theta_\vartheta(\mathbf{W}, \mathbf{V})$ with $\mathbf{W} = (d\mathbf{r}, d\mathbf{v}, d\vartheta)$, and $\mathbf{V} = \left(\dot{\mathbf{r}}, \dot{\mathbf{v}}, \dot{\vartheta}\right)$), we can write Hamiltonian (A1) as

$$H_\vartheta = P_\vartheta + \frac{m\mathbf{v}^2}{2} \tag{A4}$$

with the Hamiltonian equations identical to Equation A2. The main idea of the application of symplectic structure approach is that we can make a noncanonical change of variables (e.g., introduce $\mathbf{v}$ as a Hamiltonian variable), but keep the Hamiltonian form of equations that can be obtained from $dH = \Theta_\vartheta$ as.

$$\begin{aligned} dH_\vartheta = dP_\vartheta + m\mathbf{v}d\mathbf{v} &= m\begin{vmatrix} d\mathbf{v} & d\mathbf{r} \\ \dot{\mathbf{v}} & \dot{\mathbf{r}} \end{vmatrix} + \begin{vmatrix} dP_\vartheta & d\vartheta \\ \dot{P}_\vartheta & \dot{\vartheta} \end{vmatrix} \\ -\tfrac{e}{c}\sum_{i<j}\Gamma_{ij}\begin{vmatrix} dr_i & dr_j \\ \dot{r}_i & \dot{r}_j \end{vmatrix} &- e\mathbf{E}\begin{vmatrix} d\vartheta & d\mathbf{r} \\ \dot{\vartheta} & \dot{\mathbf{r}} \end{vmatrix} \\ = \dot{\vartheta}dP_\vartheta + m\dot{\mathbf{r}}d\mathbf{v} - \left(m\dot{\mathbf{v}} - \frac{e}{c}\left[\mathbf{v}\times\mathbf{B}\right] - e\mathbf{E}\right)d\mathbf{r} &- \left(\dot{P}_\vartheta - e\mathbf{r}\dot{\mathbf{E}}\right)d\vartheta \end{aligned} \tag{A5}$$

Equation A5 reproduces Equation A2 for $\dot{\mathbf{v}}$ and $\dot{\mathbf{r}}$, and adds two new equations: $\dot{\vartheta} = 1$ (i.e., ϑ is the time) and $\dot{P}_\vartheta = -e\mathbf{v}\mathbf{E}$ (or $\dot{P}_\vartheta = -m\mathbf{v}\dot{\mathbf{v}}$ from Equation A4; note $H = \text{const}$ in Equation A4 because after introducing ϑ Hamil-

tonian does not depend on time explicitly). Therefore, we can make any variable change through the symplectic structure, but keep the Hamiltonian form of equations with $dH = \Theta_\vartheta$ (Arnold, 1989; Arnold et al., 2006).

Then we shall transform spatial coordinates $\mathbf{r} \to \mathbf{q} = (\alpha, \beta, s)$, where $s = \mathbf{B} \cdot \mathbf{r}/B$ is the field-aligned coordinate, and α, β are normalized Euler potentials (Stern, 1970) determined as $\mathbf{B} = \bar{B}\nabla\alpha \times \nabla\beta$ ($\bar{B}$ is a typical B value). For the magnetic field configuration given by the single vector potential component we have $\beta = y$, $\alpha = A/\bar{B}$ (Birn et al., 1977). Let this coordinate transformation be determined as $\mathbf{r} = \mathbf{g}(\mathbf{q}, t)$. Then

$$\frac{e}{c}\sum_{i<j}\Gamma_{ij}dr_i \wedge dr_j = \frac{e}{c}\bar{B}d\alpha \wedge d\beta - e\sum_{i<j}\Gamma_{ij}\mathbf{h}_{ij}d\mathbf{q} \wedge d\vartheta$$
$$\mathbf{h}_{ij} = \frac{1}{c}\frac{\partial g_i}{\partial\vartheta}\nabla_\mathbf{q} g_j - \frac{1}{c}\frac{\partial g_j}{\partial\vartheta}\nabla_\mathbf{q} g_i \tag{A6}$$

and $\nabla_\mathbf{q}$ is the gradient in $\mathbf{q}$ space. We introduce 3×3 matrix $R_{ij} = \partial g_i/\partial q_j$ and rewrite $md\mathbf{v} \wedge \mathbf{r}$ as

$$md\mathbf{v} \wedge d\mathbf{r} = md\,(\mathbf{v}d\mathbf{r}) = md\,(\mathbf{v}d\mathbf{g}) = md\left(\mathbf{v}\hat{R}d\mathbf{g} + \mathbf{v}\mathbf{V}_D d\vartheta\right)$$
$$= d\left(\mathbf{p}d\mathbf{g} + \mathbf{p}\hat{R}^{-1}\mathbf{V}_D d\vartheta\right) = d\mathbf{p} \wedge d\mathbf{g} + dF \wedge d\vartheta \tag{A7}$$

where $\mathbf{p} = m\mathbf{v}\hat{R} = (p_\alpha, p_\beta, p_\parallel)$ is the momentum conjugate to $\mathbf{q}$, $\mathbf{V}_D = \partial\mathbf{g}/\partial\vartheta$, and $F = \mathbf{p}\hat{R}^{-1}\mathbf{V}_D$ (note we keep the $\mathbf{p}$ notation for the new momentum, and through the main paper text we use only $p_\parallel$).

We combine two terms of the symplectic structure to define the electric field in the new coordinates, $\tilde{\mathbf{E}}$:

$$-\ e\sum_{i<j}\Gamma_{ij}\mathbf{h}_{ij}d\mathbf{q} \wedge d\vartheta - e\mathbf{E}d\vartheta \wedge d\mathbf{r} = -e\sum_{i<j}\Gamma_{ij}\mathbf{h}_{ij}d\mathbf{q} \wedge d\vartheta - e\mathbf{E}d\vartheta \wedge \hat{R}d\mathbf{q}$$
$$=\ -e\tilde{\mathbf{E}}d\vartheta \wedge d\mathbf{q} = -ed\varphi \wedge d\vartheta \tag{A8}$$

where $\tilde{\mathbf{E}} = -\nabla_{\mathbf{q}\varphi}$, that is, the fact that Θ_ϑ is closed ($d\Theta_\vartheta = 0$) guarantees that there is only potential electric field in $\mathbf{q}$ coordinates.

Thus, Hamiltonian (A4) in new coordinates takes the form

$$H_\vartheta = P_\vartheta + \frac{1}{2m}\left(\mathbf{p}\hat{R}^{-1}\right)^2$$
$$\Theta_\vartheta = d\mathbf{p} \wedge d\mathbf{q} + d\left(F + P_\vartheta - e\varphi\right) \wedge d\vartheta - \frac{e}{c}\bar{B}d\alpha \wedge d\beta \tag{A9}$$

Here, $d\vartheta$ is the variable substituting time, and we can return to the time-dependent system by subtracting $F + P_\vartheta - e\varphi$ from the Hamiltonian:

$$H_\vartheta = \frac{1}{2m}\left(\mathbf{p}\hat{R}^{-1}\right)^2 - \mathbf{p}\hat{R}^{-1}\mathbf{V}_D + e\varphi$$
$$\Theta_\vartheta = d\mathbf{p} \wedge d\mathbf{q} - \frac{e}{c}\bar{B}d\alpha \wedge d\beta \tag{A10}$$

The velocity $\mathbf{V}_D$ is due to time-dependence of the coordinate transformation $\mathbf{r} \to \mathbf{q}$, and thus this velocity is proportional to the induction electric field, $\sim\partial\mathbf{A}/\partial t$. The direct contribution of the induction field to the electron energy is limited to the $c\mathbf{E} \times \mathbf{B}/B^2$ speed that is much smaller than electron speed and can be neglected.

Coordinates α, β describe both gyrorotation and cross-field drift, but in the case of a strong magnetic field these two types of motion are well separated. Thus, to separate them in the Hamiltonian we use the guiding-center variable transformation: $\alpha = \mathcal{A} + cp_\beta/e\bar{B}$, $\beta = Y - cp_\alpha/e\bar{B}$. The new symplectic structure is

$$\Theta_\vartheta = d\mathbf{p} \wedge d\mathbf{q} - \frac{e}{c}\bar{B}d\alpha \wedge d\beta = dp_\parallel \wedge ds + dp_\alpha \wedge d\left(\mathcal{A} + \frac{c}{e\bar{B}}p_\beta\right)$$
$$+ dp_\beta \wedge d\left(Y - \frac{c}{e\bar{B}}p_\alpha\right) - \frac{e}{c}\bar{B}d\left(\mathcal{A} + \frac{c}{e\bar{B}}p_\beta\right) \wedge d\left(Y - \frac{c}{e\bar{B}}p_\alpha\right)$$
$$= dp_\parallel \wedge ds + \frac{c}{e\bar{B}}dp_\alpha \wedge dp_\beta + \frac{e\bar{B}}{c}dY \wedge d\mathcal{A} \tag{A11}$$

This symplectic structure defines three pairs of canonically conjugate variables: $\left(p_\alpha, cp_\beta/e\bar{B}\right)$ are fast gyrorotating coordinates, $(p_\parallel, s)$ are coordinates of field-aligned motion, $\left(\mathcal{A}, e\bar{B}Y/c\right)$ are coordinates of electron slow cross-field drift. After separating three main time-scales we can introduce the adiabatic invariant corresponding to the fastest scale, gyrorotation. Using the transformation Jacobian $\hat{R}^{-1}$

$$\hat{R}^{-1} = \begin{pmatrix} B_z/\bar{B} & -\alpha_y & -B_x/\bar{B} \\ 0 & 1 & 0 \\ B_x/B & 0 & B_z/B \end{pmatrix} \tag{A12}$$

for $\nabla\alpha = (-B_z, \alpha_y, B_x)/\bar{B}$ and $\nabla s = (B_x, 0, B_z)/\bar{B}$, we rewrite the kinetic energy of Hamiltonian (A10) as

$$\begin{aligned} \left(\mathbf{p}\hat{R}^{-1}\right)^2 &= \left(-\frac{B_z}{\bar{B}}p_\alpha + \frac{B_x}{\bar{B}}p_\parallel\right)^2 + \left(\frac{B_x}{\bar{B}}p_\alpha + \frac{B_z}{\bar{B}}p_\parallel\right)^2 + (p_\beta + \alpha_y p_\alpha)^2 \\ &= p_\parallel^2 + \frac{B^2}{\bar{B}^2}p_\alpha^2 + (p_\beta + \alpha_y p_\alpha)^2 \end{aligned} \tag{A13}$$

Taking into account that $\left(p_\alpha, cp_\beta/e\bar{B}\right)$ are conjugate variables, we write the equation for the magnetic moment:

$$\begin{aligned} \mu &= \frac{1}{2\pi}\frac{c}{e\bar{B}}\oint p_\beta dp_\alpha = \frac{1}{\pi}\frac{c}{e\bar{B}}\int\sqrt{2m(H-e\varphi) - p_\parallel^2 - \frac{B^2}{\bar{B}^2}p_\alpha^2}dp_\alpha \\ &= \frac{c}{2eB}\left(2m(H-e\varphi) - p_\parallel^2\right) \end{aligned} \tag{A14}$$

Therefore, Hamiltonian (A10) can be rewritten as

$$\begin{aligned} H &= \frac{1}{2m}p_\parallel^2 + \Omega_0\mu + e\varphi \\ \Theta_\vartheta &= dp_\parallel \wedge ds + \frac{e\bar{B}}{c}dY \wedge d\mathcal{A} \end{aligned} \tag{A15}$$

where $\Omega_0 = eB/mc$ depends on $s, \mathcal{A}, Y$. Hamiltonian equations are

$$\begin{aligned} \dot{s} &= \frac{1}{m}p_\parallel, \quad \dot{p}_\parallel = -\mu\frac{\partial\Omega_0}{\partial s} \\ \dot{\mathcal{A}} &= \mu\frac{c}{e\bar{B}}\frac{\partial\Omega_0}{\partial Y}, \quad \dot{Y} = -\mu\frac{c}{e\bar{B}}\frac{\partial\Omega_0}{\partial\mathcal{A}} \end{aligned} \tag{A16}$$

By definition of α, $\mathcal{A}$ is the gyroaveraged component of the vector potential $A/\bar{B}$, and thus Equation A16 can be rewritten as

$$\begin{aligned} \dot{s} &= \frac{1}{m}p_\parallel, \quad \dot{p}_\parallel = -\mu\frac{\partial\Omega_0}{\partial s} \\ \dot{A} &= \mu\frac{c}{e}\frac{\partial\Omega_0}{\partial Y}, \quad \dot{Y} = -\mu\frac{c}{e}\frac{\partial\Omega_0}{\partial A} \end{aligned} \tag{A17}$$

where A substitutes the gyroaveraged Cartesian coordinate X.

Appendix B: Wave-Particle Resonant Interaction

A single wave-particle resonant interaction takes about a quarter of the bounce period (or much less), and electrons do not significantly change (Y, A) drift coordinates during this short time. Thus, we can freeze (Y, A) in Hamiltonian (A15) and add the field-aligned whistler wave as a perturbation of the electron bounce motion (i.e., the wave amplitude B_w is much smaller than the background magnetic field magnitude). The field-aligned wave

propagation excludes the cross-field coordinates from the wave phase, and thus the Hamiltonian for an electron bouncing and interacting with the wave can be written as (e.g., Vainchtein et al., 2018):

$$H = \frac{1}{2m}p_{\parallel}^2 + \Omega_0\mu + \sqrt{\frac{2\mu\Omega_0}{mc^2}}\frac{eB_w}{k}\sin(\phi+\theta) \tag{B1}$$

where θ is the gyrophase conjugate to μ, ϕ is the wave phase determined by $\partial\phi/\partial t = -\omega$ wave frequency and $\partial\phi/\partial s = k(s)$ wavenumber (note we consider $(d/ds)/k \ll 1$ approximation that wells work whistlers propagating in the magnetotail plasma with the current sheet thickness L much larger than the wavelength). The wave dispersion relation is given by the cold dense plasma approximation for parallel whistlers: $kd_e = (\Omega_0/\omega - 1)^{-1/2}$ and d_e is the electron inertial length determined by the plasma density that we assume to be constant within the region of a nonzero wave amplitude. This amplitude B_w is given as a function of cross-field coordinates ($B_w \to B_w \cdot G_w(A, Y)$) and/or field-aligned coordinate ($B_w \to B_w \cdot f_w(s)$). Function $G_b(A, Y)$ is determined by the dipolarizing flux bundle configuration (see the main text for details), and function $f_w(s) = s/(s + L/4)$ describes wave generation around the equator within $s \in [0, L/4]$, where we scale the generation region with the current sheet thickness L. The background magnetic field is given as $\Omega_0 = \Omega_{eq}f_b(s)G_b(A, Y)$, but for investigation of the individual wave-particle interaction we can set $G_{w,b} = 1$, because this factor only controls B_w/B_0 at the equator. Thus, the Hamiltonian equations for Hamiltonian (B1) are

$$\begin{aligned}
&\dot{s} = \frac{p_{\parallel}}{m}, \quad \dot{p}_{\parallel} \approx -\mu\frac{\partial\Omega_0}{\partial s} - \sqrt{\frac{2\mu\Omega_0}{mc^2}}eB_w\cos(\phi+\theta)\\
&\dot{\mu} \approx -\sqrt{\frac{2\mu\Omega_0}{mc^2}}\frac{eB_w}{k}\cos(\phi+\theta), \quad \dot{\theta} = \Omega_0 + \sqrt{\frac{\Omega_0}{2\mu mc^2}}\frac{eB_w}{k}\sin(\phi+\theta)
\end{aligned} \tag{B2}$$

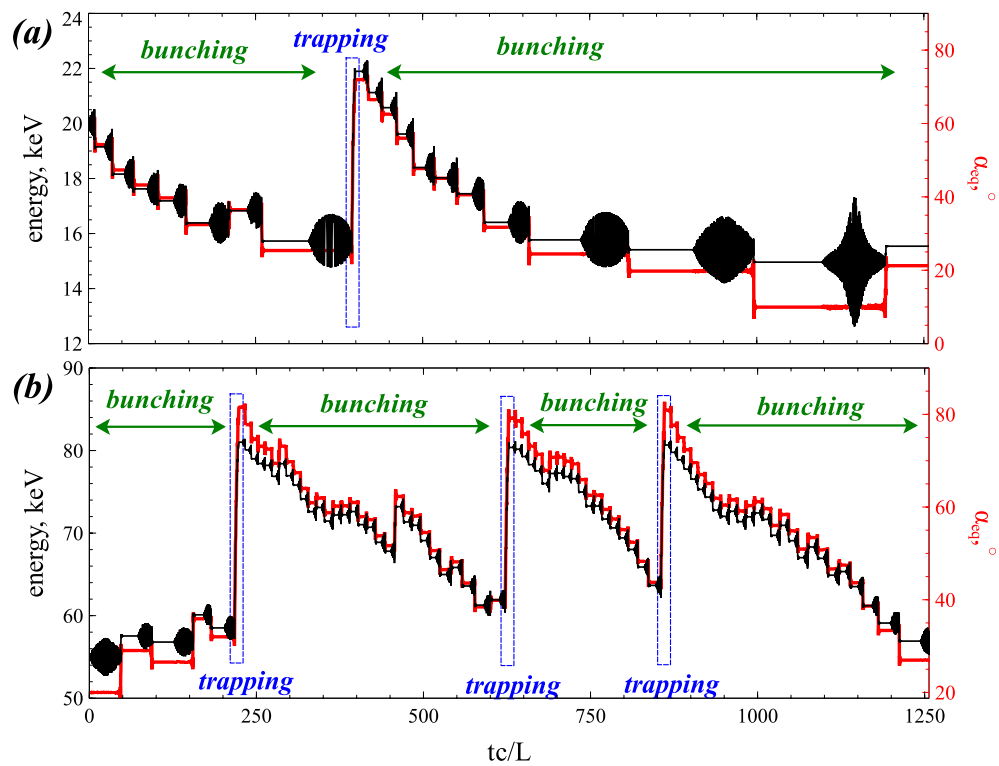

Figure B1. Energy and equatorial pitch-angle of two electrons with initial $h = 20$ keV, $\alpha_{eq} = 60°$ (a) and $h = 55$ keV, $\alpha_{eq} = 20°$ (b). Trajectories are calculated by numerical integration of Hamiltonian Equation B2 with background magnetic field 10 nT $\cdot f_b(s/L)$ and wave field 0.2 nT $\cdot f_w(s/L)$, where $L = 1R_E$ is the typical spatial scale of magnetic field inhomogeneity, f_b is given by Equation 3, $f_w = s/(s + L/4)$ for $s > 0$ and $f_w = 0$ for $s < 0$ (i.e., we consider a wave generated at the equator, $s = 0$, propagating to $s > 0$ with its amplitude increase and saturation around $L/4$ distance from the equator). Wave frequency is $0.35\Omega_{eq}$, and plasma frequency is $10\Omega_{eq}$, and Ω_{eq} is the electron equatorial gyrofrequency.

and $\dot{\phi} = k\dot{s} - \omega$. Figure B1 shows examples of electron resonances with whistlers: both trapping and bunching effects are shown. Trapping occurs rarely, but results in a significant energy increase, whereas bunching occurs at each resonant interaction and results in gradual energy decrease. The pitch-angle variation is correlated with energy variations, as it should be for the first cyclotron resonance (Shklyar & Matsumoto, 2009).

To derive the characteristics of energy change due to trapping and bunching, we follow the approach described in Neishtadt and Vasiliev (2006) and Artemyev, Neishtadt, et al. (2018). The first step is to introduce $\zeta = \phi + \theta$ as a new canonical variable through the generating function $W = (\phi + \theta)I + P_{\parallel}s$:

$$H_I = -\omega I + \frac{1}{2m}(P_{\parallel} + kI)^2 + I\Omega_0 + \sqrt{\frac{2I\Omega_0}{mc^2}}\frac{eB_w}{k}\sin\zeta \tag{B3}$$

where $I = \mu$ and $P_{\parallel} = p_{\parallel} - kI$ are new momenta conjugate to ζ and s. Hamiltonian H_I does not depend on time, and thus we have the invariant of motion $\mathcal{H} = -\omega I + h$ where h is the total energy of Hamiltonian (B1). Hamiltonian (B3) can be rewritten as

$$\begin{aligned} H_I &= \frac{k^2}{2m}(I - I_R)^2 + \frac{1}{2m}p_R\,(p_R - 2kI_R) + \sqrt{\frac{2I_R\Omega_0}{mc^2}}\frac{eB_w}{k}\sin\zeta \\ p_R &= m\frac{\omega - \Omega_0}{k}, \quad I_R = \frac{p_R - P_{\parallel}}{k} \end{aligned} \tag{B4}$$

The resonance $\partial H_I/\partial\zeta = 0$ is at $I = I_R$, where

$$\mathcal{H} = \frac{1}{2m}p_R\,(p_R - 2kI_R) = \text{const} \tag{B5}$$

determines $P_{\parallel}$ as a function of s.

We then introduce $I - I_R$ as a new momentum P_ζ through the generating function $Q = (I - I_R)\,\zeta + P_{\parallel}\tilde{s}$:

$$H_I = \frac{k^2}{2m}P_\zeta^2 + \frac{1}{2m}p_R\,(p_R - 2kI_R) + \sqrt{\frac{2I_R\Omega_0}{mc^2}}\frac{eB_w}{k}\sin\zeta \tag{B6}$$

and p_R, I_R are functions of new variables $\tilde{P}_{\parallel} = P_{\parallel} - \zeta\partial I_R/\partial s$, $\tilde{s}_{\parallel} = s + \zeta\partial I_R/\partial P_{\parallel}$. Taking into account that the ζ variation range within the resonance is $\sim\sqrt{B_w/B_0}$, we rewrite Hamiltonian (B6) as (see details in, e.g., Artemyev, Neishtadt, et al., 2018; Neishtadt, 1999; Neishtadt & Vasiliev, 2006): $H_I = \Lambda(P_{\parallel}, s) + H_\zeta$ with

$$\begin{aligned} \Lambda &= \frac{1}{2m}p_R\,(p_R - 2kI_R) \\ H_\zeta &= \frac{k^2}{2m}P_\zeta^2 + \{\Lambda, I_R\}\,\zeta + \sqrt{\frac{2I_R\Omega_0}{mc^2}}\frac{eB_w}{k}\sin\zeta \\ \{\Lambda, I_R\} &= -\frac{1}{m}\left\{p_R\,(p_R - P_{\parallel}), \frac{p_R - P_{\parallel}}{k}\right\} + \left\{\frac{1}{2m}p_R^2, \frac{p_R - P_{\parallel}}{k}\right\} \\ &= -\frac{1}{m}\,(p_R - P_{\parallel})\left(p_R\left(\frac{1}{k}\right)' - \frac{1}{k}p_R'\right) - \frac{1}{m}p_R p_R'\frac{1}{k} = P_{\parallel}\frac{\Omega_0'}{k^2} + \frac{p_R^2}{m}\frac{k'}{k^2} \end{aligned} \tag{B7}$$

where $' = \partial/\partial s$ and $p_R' = -m\Omega_0'/k^2 + p_R^2 k'/k^2 m$. Note Λ depends on old variables $P_{\parallel}$, s. For cold plasma dispersion relation with $d_e' = 0$ we can write

$$\frac{k'}{k} = \frac{1}{2}\frac{\Omega_0'}{\omega - \Omega_0} = \frac{1}{2}\frac{\Omega_0' m}{kp_R}, \quad \{\Lambda, I_R\} = \frac{1}{2}\,(2P_{\parallel} + p_R)\,\frac{\Omega_0'}{k^2} \tag{B8}$$

In Hamiltonian H_ζ variables (ζ, P_ζ) change fast, whereas variables $(s, P_{\parallel})$ can be considered as slowly changing parameters. For constant $(s, P_{\parallel})$ the phase portraits of H_ζ for different s and constant $\mathcal{H}$ are shown in Figure B2a. There are two types of phase portraits: for intermediate s we have portraits with a finite area S filled by closed trajectories, whereas for near equatorial s (where $B_w \to 0$) and for large s (where Ω_0' is large) there are only open

trajectories on the phase portrait (i.e., $S = 0$). In systems with $S = 0$ there are only electron diffusive scattering by whistlers with the diffusion rates described by quasi-linear theory (see Albert, 2010; Karpman, 1974), and we do not consider such diffusion in this study because it changes electron distribution much slower than the nonlinear wave-particle resonances do (Artemyev et al., 2019). Such nonlinear resonance effects (phase trapping and phase bunching) are fully described by $S(s)$ profile that can be rewritten as $S(h_R)$ profile with $h_R(s) = p_R^2/2m + \Omega_0 I_R$ being the resonant energy with $P_\parallel = P_\parallel(s)$ from $\mathcal{H} = -\omega I_R + h_R$ conservation

$$P_\parallel = \frac{1}{2} p_R + \frac{m\mathcal{H}}{p_R}, \quad h_R = \frac{p_R^2}{2m} + \frac{\Omega_0}{k}\left(p_R - P_\parallel\right) \tag{B9}$$

Figures B2b and B2c shows $h_R(s)$ profile and $S(h_R)$ profile.

Electrons resonating with whistlers that propagate away from the equator ($k > 0$) should move with s decrease, because $p_R < 0$. Therefore $S(s)$ first increases along the resonant electron orbit, and then (around the equator) decreases. The increase of S means that electrons on open orbits can be trapped into the region of closed trajectories (see Figure B2a), and this is the phase trapping. The probability of the phase trapping (i.e., the relative amount of trajectories trapped at given resonant s for a single resonance) is determined as (Artemyev, Vasiliev, et al., 2015; Neishtadt, 1975, 1999; Shklyar, 1981):

$$\Pi = \frac{1}{2\pi}\frac{dS}{dI} = \frac{\omega}{2\pi}\frac{dS}{dh_R} \tag{B10}$$

for $\Pi \ll 1$. Motion along the closed trajectories in the (ζ, P_ζ) plane is much faster than the phase portrait evolution due to s change. This motion corresponds to the conservation of adiabatic invariant $(2\pi)^{-1}\oint P_\zeta d\zeta$. Thus, electrons escape from the trapping at s_{escape} where $dS/dh_R < 0$ and S equals to S on the trapping. The energy gain due to trapping, Δh_{trap}, is the difference of h_R between trapping and escaping s values. Figure B3 confirms this estimate of the electron energy gain (see more results of tests in, e.g., Artemyev, Vasiliev, et al., 2015; Artemyev et al., 2020b; Itin et al., 2000; Vainchtein et al., 2018).

Nontrapped electrons (i.e., majority of resonant electrons) will be scattered (phase bunched) on the resonance with the energy decrease (for the resonant interaction with field-aligned whistlers). This energy decrease is $\Delta h_{\text{scat}} = -S/2\pi\omega$ (see derivation and testing of this equation in, e.g., Albert, 1993, 2002; Artemyev et al., 2014; Neishtadt, 1999). Therefore, profile $S(h_R)$ describes both trapping and scattering energy changes.

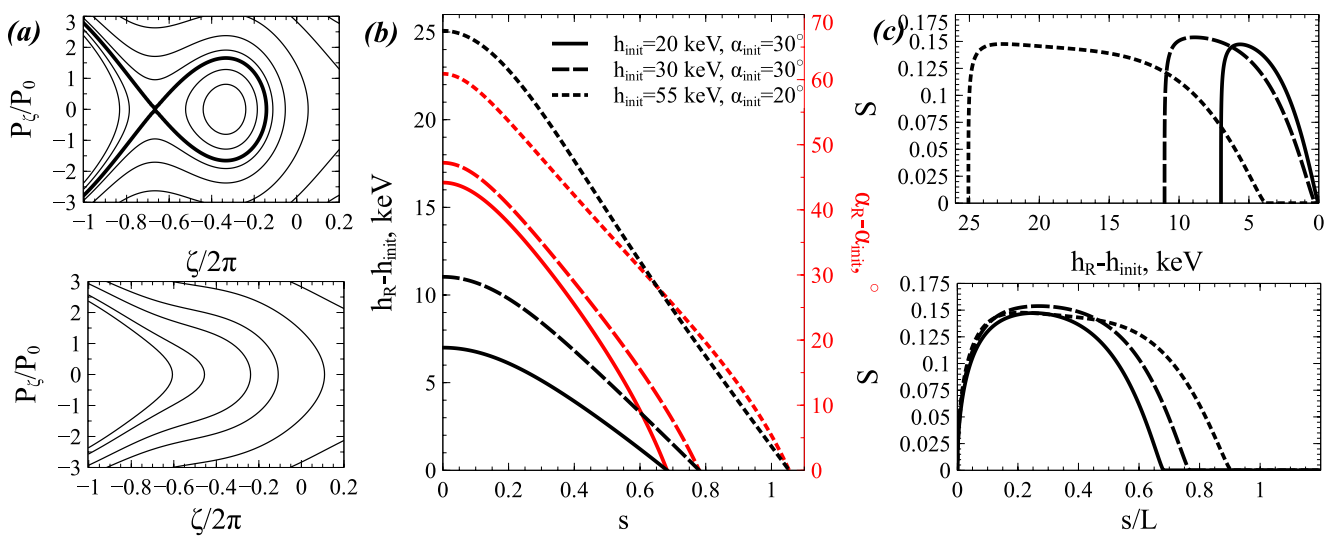

Figure B2. (a) Shows two phase portraits of Hamiltonian H_ζ from Equation B7 with $|\{\Lambda, I_R\}| = (1/2)\cdot\sqrt{2I_R\Omega_0/mc^2}eB_w/k$ (top) and $|\{\Lambda, I_R\}| = 2\cdot\sqrt{2I_R\Omega_0/mc^2}eB_w/k$ (bottom). The momentum is normalized on $P_0 = \sqrt{m|\{\Lambda, I_R\}|/k^2}$. (b) Shows h_R and α_R (pitch-angle the trapped electron) as a function of s for three initial electron energy and pitch-angles. *Note.* h_R equals the initial energy at the resonant s that is different for different h_{init}, α_{init}. (c) Shows S as a function of $h_R - h_{\text{init}}$ and s (note trapped electrons move with $p_R < 0$ from larger s toward the equator $s = 0$). System parameters are the same as in Figure B1.

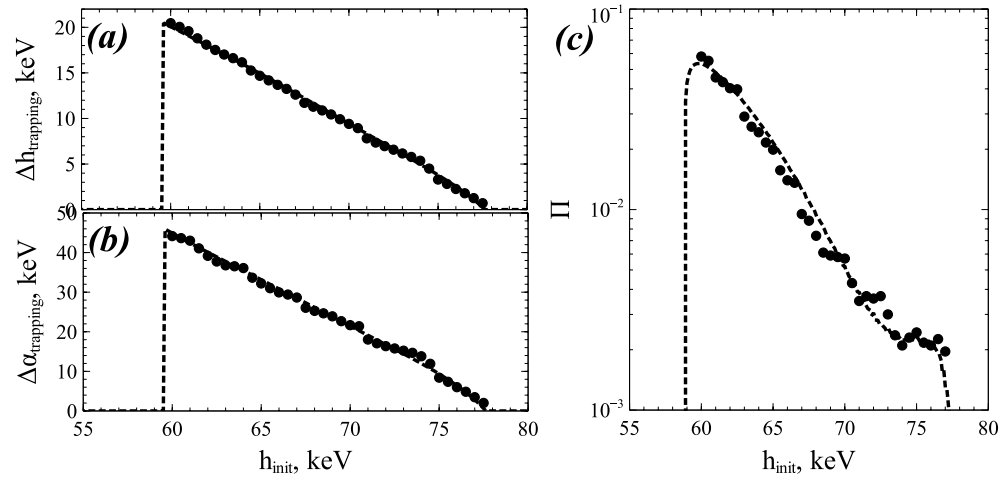

Figure B3. (a) and (b) Shows electron energy and pitch-angle change due to the phase trapping as a function of initial energy. (c) Shows the probability of trapping Π. Dashed curves are analytical results and black dots are results of numerical integration of 10^4 test particle trajectories for each h_{init}. Each trajectory integrated during the interval including one resonant interaction, and the probability of trapping is calculated as a ratio of trapped particles and total number (10^4) of particles. System parameters are the same as in Figure B1, for all electrons $\mathcal{H}$ is the same and equal to $\mathcal{H}$ for $h = 55$ keV, $\alpha_{eq} = 20°$.

Appendix C: Mapping Technique

Phase trapping is a probabilistic process and can be described by the trapping probability, Π (Neishtadt, 1975; Shklyar, 1981). The wave phase in the resonance ζ_R determines the resonant energy $h_{\zeta,R} = \zeta_R + a\sin\zeta_R$ (with $a = \sqrt{2I_R\Omega_0/mc^2eB_w/k}\,\{\Lambda, I_R\}$), and $\xi = h_{\zeta,R}/2\pi \mod 1$ defines if electrons will be trapped or scattered. Because ζ is the fast oscillating variable, a small change of ζ can change ξ value sufficiently to change the trapping to scattering (and vice versa). Therefore, we can consider ξ as a random variable and we do not trace it along the electron trajectory (see justification of this assumption in, e.g., Artemyev et al., 2020a, 2020b). This allows us to write the mapping equations for the electron energy (Artemyev, Neishtadt, et al., 2021):

$$h_{n+1} = h_n + \begin{cases} \Delta h_{trap}, & \xi \in [0, \Pi] \\ \Delta h_{scat}, & \xi \in (\Pi, 1] \end{cases} \tag{C1}$$

where n is the number of map iteration (number of resonances), ξ is the random value with the uniform distribution within [0, 1], and all map characteristics ($\Delta h_{\rm scat,trap}$ and Π) are determined by $S(h_R)$ profile. Map (C1) should be supplemented by the time iteration $t_{n+1} = t_n + \tau_b(h_n)/2$ where τ_b is the electron bounce period and there are two identical resonances for one period (one resonance for $s > 0$ and one for $s < 0$). Figure C1 shows several trajectories calculated with map (C1). These trajectories resemble well the energy profiles for test particle simulations (see Figure B1). Integration of a large ensemble of trajectories with map (C1) can describe the evolution of electron distribution for fixed $\mathcal{H}$ on the time-scale of multiple resonances (see tests in Artemyev et al., 2020b).

Map (C1) describes the resonant energy dynamics for a single wave system (wave frequency ω determines $\mathcal{H}$ value). Therefore, for the wave ensemble with the probability distribution $\mathcal{P}(\omega/\Omega_{eq}, B_w)$ this map should be generalized as (Artemyev, Neishtadt, et al., 2021):

$$h_{n+1} = h_n + \begin{cases} \Delta h_{trap,l}, & \xi \in [0, \Pi_l] \\ \Delta h_{scat,l}, & \xi \in (\Pi_l, 1] \end{cases} \tag{C2}$$
$$\alpha_{eq,n+1} = \alpha_{eq,n} + \Delta\alpha_{eq,l}\,(h_{n+1}, h_n)$$

where l is the index of $\mathcal{P}$ binning (see schematic in Figure C2) and $\Delta\alpha_{eq}$ is the solution of $\mathcal{H}_l = \text{const}$ equation (change of pitch-angle for given energy change) for ω/Ω_{eq} from l-bin.

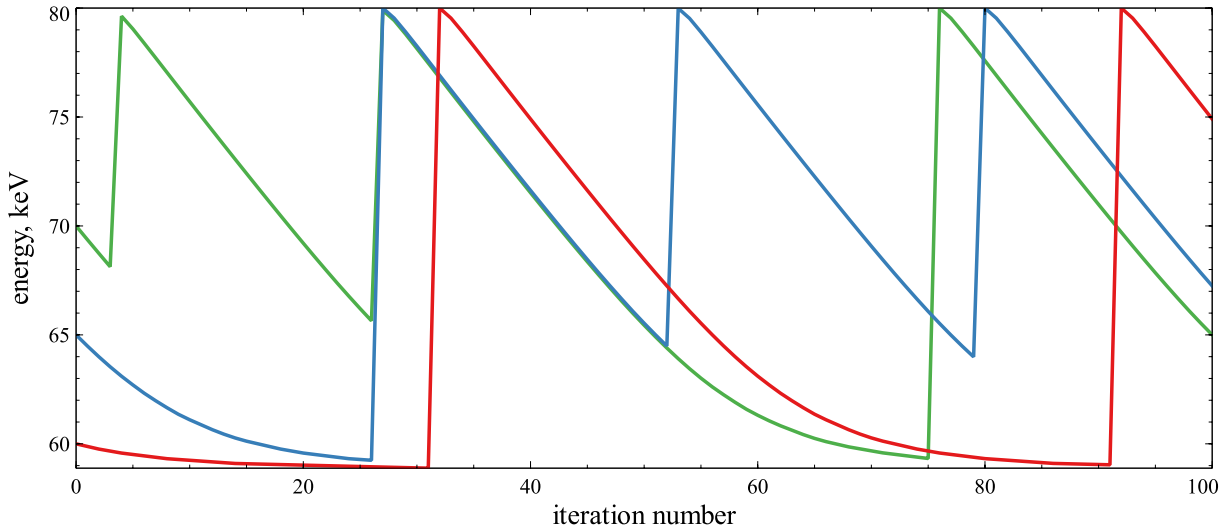

Figure C1. Three examples of test particle trajectories obtained with map (C1): energy versus map iteration number is shown. System parameters are the same as in Figure C1.

This multiple wave mapping technique resembles the Green function method (Hsieh & Omura, 2017a; Omura et al., 2015) and generalized Fokker-Planck equation (Vainchtein et al., 2018), but instead of evaluation of the entire electron distribution this map provides dynamics of individual electrons. Figure C3a shows dynamics of electron orbits for a model $\mathcal{P}(\omega/\Omega_{eq}, B_w)$ distribution. There are energy and pitch-angle gradual decrease due to the phase bunching effect and rare large amplitude increases due to the trapping. As $\mathcal{P}(\omega/\Omega_{eq}, B_w)$ contains many waves, some of these waves may not resonate with electrons for given energy and pitch-angle. Thus, the electron energy and pitch-angles do not change for each bounce period and can remain constant on some time intervals.

Running a numerical evaluation of trajectories of a large ensemble of electrons, we can trace the evolution of the electron distribution function. Figure C3b shows an example of such evolution obtained for the initial $\sim h^{-3}\sin\alpha_{eq}$ distribution and 10^6 orbits. Because the initial $\sim\sin\alpha_{eq}$ distribution has more electrons with larger pitch-angle, the resonant wave-particle interaction mostly increases the phase space density in the low pitch-angle range due to the phase bunching, whereas the acceleration of low pitch-angle electrons due to trapping remains less effective

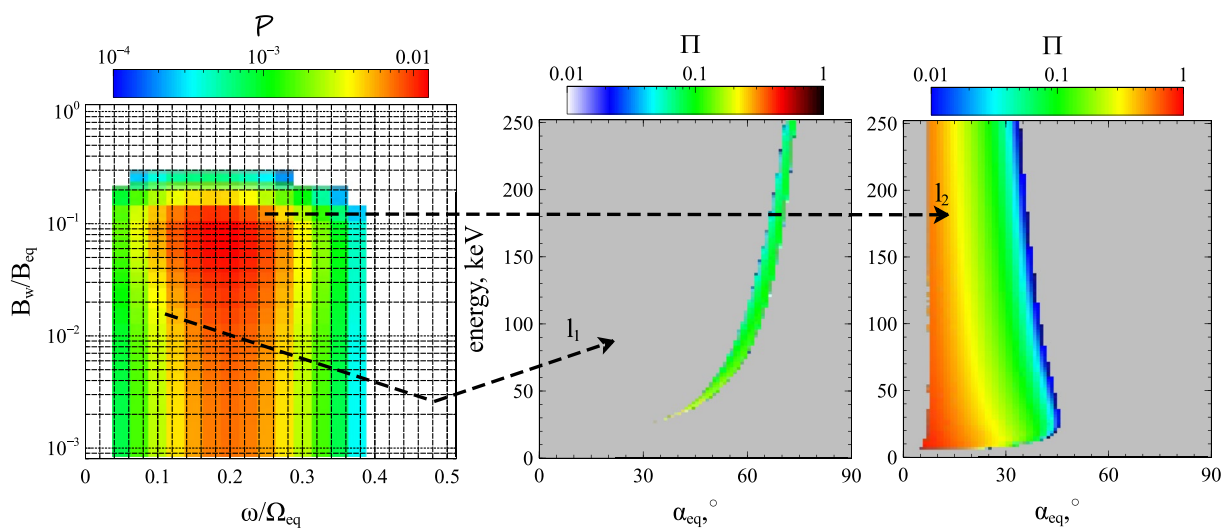

Figure C2. The example of $\mathcal{P}\left(B_w, \omega/\Omega_{eq}\right)$ distribution (left) with two $\Pi(E, \alpha_{eq})$ distributions (right) for particular bins of $(B_w, \omega/\Omega_{eq})$ space.

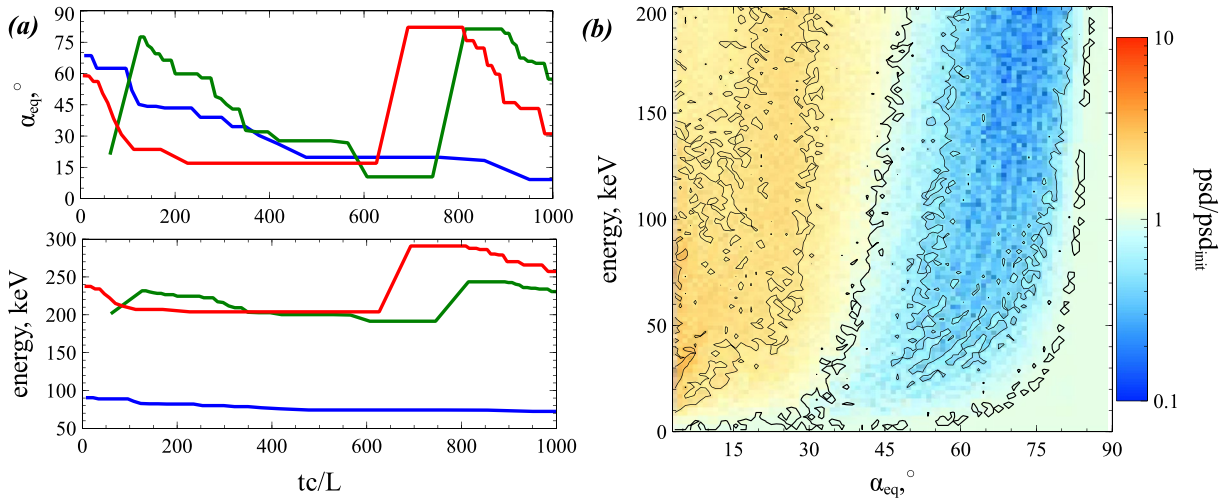

Figure C3. Results of electron energy, pitch-angle recalculation with map (C2) and $\mathcal{P}\left(\omega/\Omega_{eq}, B_w\right)$ distribution from Figure C2. (a) Show three examples of electron trajectories with the iteration number n recalculated to the time as $t_n = t_{n-1} + \tau_b(h, \alpha)/2$ and τ_{bounce} is the bounce period of electron motion in the $f_b(s)$ magnetic field given by Equation 3. b Shows the change of the electron phase space density in the (energy and pitch-angle) space for 10^6 test trajectories and time $100 \cdot R/c$. The initial phase space density is $\sim h^{-3} \sin\alpha_{\text{eq}}$.

for the phase space density evolution. This example shows that the mapping technique reproduces the main effect of the wave-particle resonant interaction: the smoothing and reduction of the phase space density gradients along the resonant curves (see discussion in Artemyev et al., 2016, 2019).

Data Availability Statement

ELFIN data is available at http://themis-data.igpp.ucla.edu/ela/. THEMIS data is available at http://themis.ssl.berkeley.edu. Data access and processing was done using SPEDAS V4.1, see Angelopoulos et al. (2019).

Acknowledgments
We are grateful to Dr. D. Mourenas for valuable discussion of this study. We are grateful to NASA's CubeSat Launch Initiative for ELFIN's successful launch in the desired orbits. We acknowledge early support of ELFIN project by the AFOSR, under its University Nanosat Program, UNP-8 project, contract FA9453-12-D-0285, and by the California Space Grant program. We acknowledge critical contributions of numerous volunteer ELFIN team student members. A. V. Artemyev and V. Angelopoulos acknowledge support by NASA awards 80NSSC20K1578, 80NSSC19K0266, 80NSSC21K0729, NNX14AN68G, and NSF grants AGS-1242918, AGS-2019950, and AGS-1914594. A. I. Neishtadt acknowledges support by Leverhulme Trust project RPG-2018-143.

References

Agapitov, O. V., Artemyev, A. V., Mourenas, D., Mozer, F. S., & Krasnoselskikh, V. (2015). Empirical model of lower band chorus wave distribution in the outer radiation belt. *Journal of Geophysical Research: Space Physics*, *120*, 10425–10442. https://doi.org/10.1002/2015JA021829

Agapitov, O. V., Mourenas, D., Artemyev, A. V., Mozer, F. S., Hospodarsky, G., Bonnell, J., & Krasnoselskikh, V. (2018). Synthetic empirical chorus wave model from combined Van Allen Probes and cluster statistics. *Journal of Geophysical Research: Space pyhysics*, *123*(1), 297–314. https://doi.org/10.1002/2017JA024843

Albert, J. M. (1993). Cyclotron resonance in an inhomogeneous magnetic field. *Physics of Fluids B*, *5*, 2744–2750. https://doi.org/10.1063/1.860715

Albert, J. M. (2001). Comparison of pitch angle diffusion by turbulent and monochromatic whistler waves. *Journal of Geophysical Research: Atmospheres*, *106*, 8477–8482. https://doi.org/10.1029/2000JA000304

Albert, J. M. (2002). Nonlinear interaction of outer zone electrons with VLF waves. *Geophysical Research Letters*, *29*(8). https://doi.org/10.1029/2001GL013941

Albert, J. M. (2008). Efficient approximations of quasi-linear diffusion coefficients in the radiation belts. *Journal of Geophysical Research*, *113*, 6208. https://doi.org/10.1029/2007JA012936

Albert, J. M. (2010). Diffusion by one wave and by many waves. *Journal of Geophysical Research: Space Physics*, *115*(8), A00F05. https://doi.org/10.1029/2009JA014732

Allanson, O., Watt, C. E. J., Allison, H. J., & Ratcliffe, H. (2021). Electron diffusion and advection during nonlinear interactions with whistler mode waves. *Journal of Geophysical Research: Space Physics*, *126*(5), e28793. https://doi.org/10.1029/2020JA028793

Allanson, O., Watt, C. E. J., Ratcliffe, H., Allison, H. J., Meredith, N. P., Bentley, S. N., Glauert, S. A., et al. (2020). Particle-in-cell experiments examine electron diffusion by whistler-mode waves: 2. Quasi-linear and nonlinear dynamics. *Journal of Geophysical Research: Space Physics*, *125*(7), e27949. https://doi.org/10.1029/2020JA027949

An, X., Bortnik, J., & Zhang, X.-J. (2021). Nonlinear Landau resonant interaction between kinetic Alfvén waves and thermal electrons: Excitation of time domain structures. *Journal of Geophysical Research: Space Physics*, *126*(1), e28643. https://doi.org/10.1029/2020JA028643

Anderson, B. J., Decker, R. B., Paschalidis, N. P., & Sarris, T. (1997). Onset of nonadiabatic particle motion in the near-Earth magnetotail. *Journal of Geophysical Research*, *102*, 17553–17570. https://doi.org/10.1029/97JA00798

Andreeva, V. A., & Tsyganenko, N. A. (2019). Empirical modeling of the geomagnetosphere for SIR and CME-driven magnetic storms. *Journal of Geophysical Research: Space Physics*, *124*(7), 5641–5662. https://doi.org/10.1029/2018JA026008

Andronov, A. A., & Trakhtengerts, V. Y. (1964). Kinetic instability of the Earth's outer radiation belt. *Geomagnetism and Aeronomy*, *4*, 233–242.

Angelopoulos, V. (2008). The THEMIS mission. *Space Science Reviews*, *141*, 5–34. https://doi.org/10.1007/s11214-008-9336-1

Angelopoulos, V., Cruce, P., Drozdov, A., Grimes, E. W., Hatzigeorgiu, N., King, D. A., et al. (2019). The space physics environment data analysis system (SPEDAS). *Space Science Reviews*, *215*, 9. https://doi.org/10.1007/s11214-018-0576-4

Angelopoulos, V., Kennel, C. F., Coroniti, F. V., Pellat, R., Spence, H. E., Kivelson, M. G., et al. (1993). Characteristics of ion flow in the quiet state of the inner plasma sheet. *Geophysical Research Letters*, *20*, 1711–1714. https://doi.org/10.1029/93GL00847

Angelopoulos, V., Runov, A., Zhou, X. Z., Turner, D. L., Kiehas, S. A., Li, S. S., & Shinohara, I. (2013). Electromagnetic energy Conversion at reconnection fronts. *Science*, *341*, 1478–1482. https://doi.org/10.1126/science.1236992

Angelopoulos, V., Sibeck, D., Carlson, C. W., McFadden, J. P., Larson, D., Lin, R. P., et al. (2008). First results from the THEMIS mission. *Space Science Reviews*, *141*, 453–476. https://doi.org/10.1007/s11214-008-9378-4

Angelopoulos, V., Tsai, E., Bingley, L., Shaffer, C., Turner, D. L., Runov, A., et al. (2020). The ELFIN mission. *Space Science Reviews*, *216*(5), 103. https://doi.org/10.1007/s11214-020-00721-7

Arnold, V. I. (1989). *Mathematical methods of classical mechanics* (2rd ed.). Springer-Verlag.

Arnold, V. I., Kozlov, V. V., & Neishtadt, A. I. (2006). *Mathematical aspects of classical and celestial mechanics* (3rd ed.). Springer-Verlag.

Artemyev, A. V. (2014). Charged-particle acceleration in braking plasma jets. *Physical Review E*, *89*(3), 033108. https://doi.org/10.1103/PhysRevE.89.033108

Artemyev, A. V., Angelopoulos, V., Hietala, H., Runov, A., & Shinohara, I. (2017). Ion density and temperature profiles along (X_{GSM}) and across (Z_{GSM}) the magnetotail as observed by THEMIS, Geotail, and ARTEMIS. *Journal of Geophysical Research: Space Physics*, *122*, 1590–1599. https://doi.org/10.1002/2016JA023710

Artemyev, A. V., Demekhov, A. G., Zhang, X. J., Angelopoulos, V., Mourenas, D., Fedorenko, Y. V., & Shinohara, I. (2021). Role of ducting in relativistic electron loss by whistler-mode wave scattering. *Journal of Geophysical Research: Space Physics*, *126*(11), e29851. https://doi.org/10.1029/2021JA029851

Artemyev, A. V., Neishtadt, A. I., Vainchtein, D. L., Vasiliev, A. A., Vasko, I. Y., & Zelenyi, L. M. (2018). Trapping (capture) into resonance and scattering on resonance: Summary of results for space plasma systems. *Communications in Nonlinear Science and Numerical Simulations*, *65*, 111–160. https://doi.org/10.1016/j.cnsns.2018.05.004

Artemyev, A. V., Neishtadt, A. I., & Vasiliev, A. A. (2019). Kinetic equation for nonlinear wave-particle interaction: Solution properties and asymptotic dynamics. *Physica D: Nonlinear Phenomena*, *393*, 1–8. https://doi.org/10.1016/j.physd.2018.12.007

Artemyev, A. V., Neishtadt, A. I., & Vasiliev, A. A. (2020a). A map for systems with resonant trappings and scatterings. *Regular & Chaotic Dynamics*, *25*(1), 2–10. https://doi.org/10.1134/S1560354720010025

Artemyev, A. V., Neishtadt, A. I., & Vasiliev, A. A. (2020b). Mapping for nonlinear electron interaction with whistler-mode waves. *Physics of Plasmas*, *27*(4), 042902. https://doi.org/10.1063/1.5144477

Artemyev, A. V., Neishtadt, A. I., Vasiliev, A. A., & Mourenas, D. (2016). Kinetic equation for nonlinear resonant wave-particle interaction. *Physics of Plasmas*, *23*(9), 090701. https://doi.org/10.1063/1.4962526

Artemyev, A. V., Neishtadt, A. I., Vasiliev, A. A., & Mourenas, D. (2017). Probabilistic approach to nonlinear wave-particle resonant interaction. *Physical Review E*, *95*(2), 023204. https://doi.org/10.1103/PhysRevE.95.023204

Artemyev, A. V., Neishtadt, A. I., Vasiliev, A. A., Zhang, X.-J., Mourenas, D., & Vainchtein, D. (2021). Long-term dynamics driven by resonant wave-particle interactions: From Hamiltonian resonance theory to phase space mapping. *Journal of Plasma Physics*, *87*(2), 835870201. https://doi.org/10.1017/S0022377821000246

Artemyev, A. V., Orlova, K. G., Mourenas, D., Agapitov, O. V., & Krasnoselskikh, V. V. (2013). Electron pitch-angle diffusion: Resonant scattering by waves vs. nonadiabatic effects. *Annales Geophysicae*, *31*, 1485–1490. https://doi.org/10.5194/angeo-31-1485-2013

Artemyev, A. V., Petrukovich, A. A., Nakamura, R., & Zelenyi, L. M. (2011). Cluster statistics of thin current sheets in the Earth magnetotail: Specifics of the dawn flank, proton temperature profiles and electrostatic effects. *Journal of Geophysical Research: Space Physics*, *116*, A0923. https://doi.org/10.1029/2011JA016801

Artemyev, A. V., Petrukovich, A. A., Nakamura, R., & Zelenyi, L. M. (2012). Adiabatic electron heating in the magnetotail current sheet: Cluster observations and analytical models. *Journal of Geophysical Research: Atmospheres*, *117*, A06219. https://doi.org/10.1029/2012JA017513

Artemyev, A. V., Rankin, R., & Blanco, M. (2015a). Electron trapping and acceleration by kinetic Alfven waves in the inner magnetosphere. *Journal of Geophysical Research: Space Physics*, *120*, 10. https://doi.org/10.1002/2015JA021781

Artemyev, A. V., Vasiliev, A. A., Mourenas, D., Agapitov, O. V., & Krasnoselskikh, V. V. (2014). Electron scattering and nonlinear trapping by oblique whistler waves: The critical wave intensity for nonlinear effects. *Physics of Plasmas*, *21*(10), 102903. https://doi.org/10.1063/1.4897945

Artemyev, A. V., Vasiliev, A. A., Mourenas, D., Neishtadt, A. I., Agapitov, O. V., & Krasnoselskikh, V. (2015b). Probability of relativistic electron trapping by parallel and oblique whistler-mode waves in Earth's radiation belts. *Physics of Plasmas*, *22*(11), 112903. https://doi.org/10.1063/1.4935842

Artemyev, A. V., & Zelenyi, L. M. (2013). Kinetic structure of current sheets in the Earth magnetotail. *Space Science Reviews*, *178*, 419–440. https://doi.org/10.1007/s11214-012-9954-5

Artemyev, A. V., Zelenyi, L. M., Petrukovich, A. A., & Nakamura, R. (2011). Hot electrons as tracers of large-scale structure of magnetotail current sheets. *Geophysical Research Letters*, *38*, L14102. https://doi.org/10.1029/2011GL047979

Artemyev, A. V., Zhang, X. J., Angelopoulos, V., Runov, A., Spence, H. E., & Larsen, B. A. (2018). Plasma anisotropies and currents in the near-Earth plasma sheet and inner magnetosphere. *Journal of Geophysical Research: Space Physics*, *123*(7), 5625–5639. https://doi.org/10.1029/2018JA025232

Ashour-Abdalla, M., El-Alaoui, M., Goldstein, M. L., Zhou, M., Schriver, D., Richard, R., et al. (2011). Observations and simulations of non-local acceleration of electrons in magnetotail magnetic reconnection events. *Nature Physics*, *7*, 360–365. https://doi.org/10.1038/nphys1903

Auster, H. U., Glassmeier, K. H., Magnes, W., Aydogar, O., Baumjohann, W., Constantinescu, D., et al. (2008). The THEMIS fluxgate magnetometer. *Space Science Reviews*, *141*, 235–264. https://doi.org/10.1007/s11214-008-9365-9

Baumjohann, W. (2002). Modes of convection in the magnetotail. *Physics of Plasmas*, *9*, 3665–3667. https://doi.org/10.1063/1.1499116

Bell, T. F. (1984). The nonlinear gyroresonance interaction between energetic electrons and coherent VLF waves propagating at an arbitrary angle with respect to the Earth's magnetic field. *Journal of Geophysical Research*, *89*, 905–918. https://doi.org/10.1029/JA089iA02p00905

Bell, T. F., Inan, U. S., Bortnik, J., & Scudder, J. D. (2002). The Landau damping of magnetospherically reflected whistlers within the plasmasphere. *Geophysical Research Letters*, *29*, 1733. https://doi.org/10.1029/2002GL014752

Benkadda, S., Sen, A., & Shklyar, D. R. (1996). Chaotic dynamics of charged particles in the field of two monochromatic waves in a magnetized plasma. *Chaos*, *6*(3), 451–460. https://doi.org/10.1063/1.166187

Birmingham, T. J. (1984). Pitch angle diffusion in the Jovian magnetodisc. *Journal of Geophysical Research: Space Physics*, *89*, 2699–2707. https://doi.org/10.1029/JA089iA05p02699

Birn, J. (1989). Three-dimensional equilibria for the extended magnetotail and the generation of field-aligned current sheets. *Journal of Geophysical Research*, *94*, 252–260. https://doi.org/10.1029/JA094iA01p00252

Birn, J., Artemyev, A. V., Baker, D. N., Echim, M., Hoshino, M., & Zelenyi, L. M. (2012). Particle acceleration in the magnetotail and aurora. *Space Science Reviews*, *173*, 49–102. https://doi.org/10.1007/s11214-012-9874-4

Birn, J., Hesse, M., Nakamura, R., & Zaharia, S. (2013). Particle acceleration in dipolarization events. *Journal of Geophysical Research: Space Physics*, *118*, 1960–1971. https://doi.org/10.1002/jgra.50132

Birn, J., Runov, A., & Hesse, M. (2014). Energetic electrons in dipolarization events: Spatial properties and anisotropy. *Journal of Geophysical Research: Space Physics*, *119*(5), 3604–3616. https://doi.org/10.1002/2013JA019738

Birn, J., Runov, A., & Hesse, M. (2015). Energetic ions in dipolarization events. *Journal of Geophysical Research: Space Physics*, *120*, 7698–7717. https://doi.org/10.1002/2015JA021372

Birn, J., Sommer, R. R., & Schindler, K. (1977). Self-consistent theory of the quiet magnetotail in three dimensions. *Journal of Geophysical Research*, *82*, 147–154. https://doi.org/10.1029/JA082i001p00147

Bortnik, J., Thorne, R. M., Meredith, N. P., & Santolik, O. (2007). Ray tracing of penetrating chorus and its implications for the radiation belts. *Geophysical Research Letters*, *34*, L15109. https://doi.org/10.1029/2007GL030040

Breuillard, H., Le Contel, O., Retino, A., Chasapis, A., Chust, T., Mirioni, L., et al. (2016). Multispacecraft analysis of dipolarization fronts and associated whistler wave emissions using MMS data. *Geophysical Research Letters*, *43*, 7279–7286. https://doi.org/10.1002/2016GL069188

Breuillard, H., Zaliznyak, Y., Agapitov, O., Artemyev, A., Krasnoselskikh, V., & Rolland, G. (2013). Spatial spreading of magnetospherically reflected chorus elements in the inner magnetosphere. *Annales Geophysicae*, *31*, 1429–1435. https://doi.org/10.5194/angeo-31-1429-2013

Breuillard, H., Zaliznyak, Y., Krasnoselskikh, V., Agapitov, O., Artemyev, A., & Rolland, G. (2012). Chorus wave-normal statistics in the Earth's radiation belts from ray tracing technique. *Annales Geophysicae*, *30*, 1223–1233. https://doi.org/10.5194/angeo-30-1223-2012

Büchner, J., & Zelenyi, L. M. (1989). Regular and chaotic charged particle motion in magnetotaillike field reversals. I—Basic theory of trapped motion. *Journal of Geophysical Research*, *94*, 11821–11842. https://doi.org/10.1029/JA094iA09p11821

Cairns, I. H., & McMillan, B. F. (2005). Electron acceleration by lower hybrid waves in magnetic reconnection regions. *Physics of Plasmas*, *12*(10), 102110. https://doi.org/10.1063/1.2080567

Cary, J. R., & Brizard, A. J. (2009). Hamiltonian theory of guiding-center motion. *Reviews of Modern Physics*, *81*, 693–738. https://doi.org/10.1103/RevModPhys.81.693

Chen, L., Thorne, R. M., Li, W., & Bortnik, J. (2013). Modeling the wave normal distribution of chorus waves. *Journal of Geophysical Research: Space Physics*, *118*, 1074–1088. https://doi.org/10.1029/2012JA018343

Cheng, L., Lin, Y., Perez, J. D., Johnson, J. R., & Wang, X. (2020). Kinetic Alfvén waves from magnetotail to the ionosphere in global hybrid simulation associated with fast flows. *Journal of Geophysical Research: Space Physics*, *125*(2), e27062. https://doi.org/10.1029/2019JA027062

Chirikov, B. V. (1979). A universal instability of many-dimensional oscillator systems. *Physics Reports*, *52*, 263–379. https://doi.org/10.1016/0370-1573(79)90023-1

Cohen, R. H., Rowlands, G., & Foote, J. H. (1978). Nonadiabaticity in mirror machines. *Physics of Fluids*, *21*, 627–644. https://doi.org/10.1063/1.862271

Crabtree, C., Ganguli, G., & Tejero, E. (2017). Analysis of self-consistent nonlinear wave-particle interactions of whistler waves in laboratory and space plasmas. *Physics of Plasmas*, *24*(5), 056501. https://doi.org/10.1063/1.4977539

Cully, C. M., Ergun, R. E., Stevens, K., Nammari, A., & Westfall, J. (2008). The THEMIS digital fields board. *Space Science Reviews*, *141*, 343–355. https://doi.org/10.1007/s11214-008-9417-1

Damiano, P. A., Johnson, J. R., & Chaston, C. C. (2015). Ion temperature effects on magnetotail Alfvén wave propagation and electron energization. *Journal of Geophysical Research: Space Physics*, *120*, 5623–5632. https://doi.org/10.1002/2015JA021074

Damiano, P. A., Johnson, J. R., & Chaston, C. C. (2016). Ion gyroradius effects on particle trapping in kinetic Alfvn waves along auroral field lines. *Journal of Geophysical Research*, *121*(11), 10831–10844. https://doi.org/10.1002/2016JA022566

Delcourt, D. C., Martin, R. F., Jr., & Alem, F. (1994). A simple model of magnetic moment scattering in a field reversal. *Geophysical Research Letters*, *21*, 1543–1546. https://doi.org/10.1029/94GL01291

Delcourt, D. C., Sauvaud, J. A., Martin, R. F., & Moore, T. E. (1995). Gyrophase effects in the centrifugal impulse model of particle motion in the magnetotail. *Journal of Geophysical Research*, *100*, 17211–17220. https://doi.org/10.1029/95JA00657

Demekhov, A. G. (2011). Generation of VLF emissions with the increasing and decreasing frequency in the magnetosperic cyclotron maser in the backward wave oscillator regime. *Radiophysics and Quantum Electronics*, *53*, 609–622. https://doi.org/10.1007/s11141-011-9256-x

Demekhov, A. G., Trakhtengerts, V. Y., Rycroft, M. J., & Nunn, D. (2006). Electron acceleration in the magnetosphere by whistler-mode waves of varying frequency. *Geomagnetism and Aeronomy*, *46*, 711–716. https://doi.org/10.1134/S0016793206060053

Drummond, W. E., & Pines, D. (1962). Nonlinear stability of plasma oscillations. *Nuclear Fusion*, *3*, 1049–1058. Retrieved from https://www-thphys.physics.ox.ac.uk/people/AlexanderSchekochihin/notes/PlasmaClassics/drummond_pines62.pdf

Dubyagin, S., Apatenkov, S., Gordeev, E., Ganushkina, N., & Zheng, Y. (2021). Conditions of loss cone filling by scattering on the curved field lines for 30 keV protons during geomagnetic storm as inferred from numerical trajectory tracing. *Journal of Geophysical Research: Space Physics*, *126*(1), e28490. https://doi.org/10.1029/2020JA028490

Dubyagin, S., Sergeev, V., Apatenkov, S., Angelopoulos, V., Runov, A., Nakamura, R., et al. (2011). Can flow bursts penetrate into the inner magnetosphere? *Geophysical Research Letters*, *38*, 8102. https://doi.org/10.1029/2011GL047016

Elkington, S. R., Chan, A. A., Jaynes, A. N., Malaspina, D., & Albert, J. (2019). *K2: Towards a comprehensive simulation framework of the Van Allen radiation belts*. (Vol. 2019, SM44B-01). AGU Fall Meeting Abstracts.

Eshetu, W. W., Lyon, J. G., Hudson, M. K., & Wiltberger, M. J. (2018). Pitch angle scattering of energetic electrons by BBFs. *Journal of Geophysical Research: Space Physics*, *123*(11), 9265–9274. https://doi.org/10.1029/2018JA025788

Eshetu, W. W., Lyon, J. G., Hudson, M. K., & Wiltberger, M. J. (2019). Simulations of electron energization and injection by BBFs using high-resolution LFM MHD fields. *Journal of Geophysical Research: Space Physics*, *124*(2), 1222–1238. https://doi.org/10.1029/2018JA025789

Fu, H. S., Khotyaintsev, Y. V., André, M., & Vaivads, A. (2011). Fermi and betatron acceleration of suprathermal electrons behind dipolarization fronts. *Geophysical Research Letters*, *381*, 16104. https://doi.org/10.1029/2011GL048528

Fu, H. S., Khotyaintsev, Y. V., Vaivads, A., André, M., Sergeev, V. A., Huang, S. Y., et al. (2012). Pitch angle distribution of suprathermal electrons behind dipolarization fronts: A statistical overview. *Journal of Geophysical Research: Space Physics*, *117*, 12221. https://doi.org/10.1029/2012JA018141

Fu, H. S., Khotyaintsev, Y. V., Vaivads, A., Retinò, A., & André, M. (2013). Energetic electron acceleration by unsteady magnetic reconnection. *Nature Physics*, *9*, 426–430. https://doi.org/10.1038/nphys2664

Fu, X., Cowee, M. M., Friedel, R. H., Funsten, H. O., Gary, S. P., Hospodarsky, G. B., et al. (2014). Whistler anisotropy instabilities as the source of banded chorus: Van Allen Probes observations and particle-in-cell simulations. *Journal of Geophysical Research: Space Physics*, *119*, 8288–8298. https://doi.org/10.1002/2014JA020364

Furuya, N., Omura, Y., & Summers, D. (2008). Relativistic turning acceleration of radiation belt electrons by whistler mode chorus. *Journal of Geophysical Research: Space Physics*, *113*, 4224. https://doi.org/10.1029/2007JA012478

Gabrielse, C., Angelopoulos, V., Harris, C., Artemyev, A., Kepko, L., & Runov, A. (2017). Extensive electron transport and energization via multiple, localized dipolarizing flux bundles. *Journal of Geophysical Research: Space Physics*, *122*, 5059–5076. https://doi.org/10.1002/2017JA023981

Gabrielse, C., Angelopoulos, V., Runov, A., & Turner, D. L. (2012). The effects of transient, localized electric fields on equatorial electron acceleration and transport toward the inner magnetosphere. *Journal of Geophysical Research: Space Physics*, *117*, 10213. https://doi.org/10.1029/2012JA017873

Gabrielse, C., Angelopoulos, V., Runov, A., & Turner, D. L. (2014). Statistical characteristics of particle injections throughout the equatorial magnetotail. *Journal of Geophysical Research: Space Physics*, *119*, 2512–2535. https://doi.org/10.1002/2013JA019638

Gabrielse, C., Harris, C., Angelopoulos, V., Artemyev, A., & Runov, A. (2016). The role of localized inductive electric fields in electron injections around dipolarizing flux bundles. *Journal of Geophysical Research: Space Physics*, *121*, 9560–9585. https://doi.org/10.1002/2016JA023061

Gabrielse, C., Spanswick, E., Artemyev, A., Nishimura, Y., Runov, A., Lyons, L., et al. (2019). Utilizing the Heliophysics/Geospace System observatory to understand particle injections: Their scale sizes and propagation directions. *Journal of Geophysical Research: Space Physics*, *124*(7), 5584–5609. https://doi.org/10.1029/2018JA025588

Gan, L., Li, W., Ma, Q., Artemyev, A. V., & Albert, J. M. (2020). Unraveling the formation mechanism for the bursts of electron butterfly distributions: Test particle and quasilinear simulations. *Geophysical Research Letters*, *47*(21), e90749. https://doi.org/10.1029/2020GL090749

Gardner, C. S. (1959). Adiabatic invariants of periodic classical systems. *Physical Review*, *115*, 791–794. https://doi.org/10.1103/PhysRev.115.791

Génot, V., Louarn, P., & Mottez, F. (2004). Alfvén wave interaction with inhomogeneous plasmas: Acceleration and energy cascade towards small-scales. *Annales Geophysicae*, *22*, 2081–2096. https://doi.org/10.5194/angeo-22-2081-2004

Ghaffari, R., Cully, C. M., & Gabrielse, C. (2021). Statistical study of whistler-mode waves and expected pitch angle diffusion rates during dispersionless electron injections. *Geophysical Research Letters*, *48*(17), e2021GL094085. https://doi.org/10.1029/2021GL094085

Glauert, S. A., & Horne, R. B. (2005). Calculation of pitch angle and energy diffusion coefficients with the PADIE code. *Journal of Geophysical Research: Space Physics*, *110*, 4206. https://doi.org/10.1029/2004JA010851

Grigorenko, E. E., Malykhin, A. Y., Shklyar, D. R., Fadanelli, S., Lavraud, B., Panov, E. V., et al. (2020). Investigation of electron distribution functions associated with whistler waves at dipolarization fronts in the Earth's magnetotail: MMS observations. *Journal of Geophysical Research: Space Physics*, *125*(9), e28268. https://doi.org/10.1029/2020JA028268

Howard, J. E. (1971). Nonadiabatic particle motion in cusped magnetic fields. *Physics of Fluids*, *14*, 2378–2384. https://doi.org/10.1063/1.1693344

Hsieh, Y.-K., Kubota, Y., & Omura, Y. (2020). Nonlinear evolution of radiation belt electron fluxes interacting with oblique whistler mode chorus emissions. *Journal of Geophysical Research: Space Physics*, *125*(2), e2019JA027465. https://doi.org/10.1029/2019ja027465

Hsieh, Y.-K., & Omura, Y. (2017a). Nonlinear dynamics of electrons interacting with oblique whistler mode chorus in the magnetosphere. *Journal of Geophysical Research: Space Physics*, *122*, 675–694. https://doi.org/10.1002/2016JA023255

Hsieh, Y.-K., & Omura, Y. (2017b). Study of wave-particle interactions for whistler mode waves at oblique angles by utilizing the gyroaveraging method. *Radio Science*, *52*(10), 1268–1281. https://doi.org/10.1002/2017RS006245

Hwang, K.-J., Goldstein, M. L., Lee, E., & Pickett, J. S. (2011). Cluster observations of multiple dipolarization fronts. *Journal of Geophysical Research: Atmospheres*, *116*, A00I32. https://doi.org/10.1029/2010JA015742

Imhof, W. L., Reagan, J. B., & Gaines, E. E. (1979). Studies of the sharply defined L dependent energy threshold for isotropy at the midnight trapping boundary. *Journal of Geophysical Research*, *84*, 6371–6384. https://doi.org/10.1029/JA084iA11p06371

Itin, A. P., Neishtadt, A. I., & Vasiliev, A. A. (2000). Captures into resonance and scattering on resonance in dynamics of a charged relativistic particle in magnetic field and electrostatic wave. *Physica D: Nonlinear Phenomena*, *141*, 281–296. https://doi.org/10.1016/S0167-2789(00)00039-7

Kamaletdinov, S. R., Yushkov, E. V., Artemyev, A. V., Lukin, A. S., & Vasko, I. Y. (2020). Superthin current sheets supported by anisotropic electrons. *Physics of Plasmas*, *27*(8), 082904. https://doi.org/10.1063/5.0018063

Karpman, V. I. (1974). Nonlinear effects in the ELF waves propagating along the magnetic field in the magnetosphere. *Space Science Reviews*, *16*, 361–388. https://doi.org/10.1007/BF00171564

Karpman, V. I., & Shkliar, D. R. (1977). Particle precipitation caused by a single whistler-mode wave injected into the magnetosphere. *Planetary and Space Science*, *25*, 395–403. https://doi.org/10.1016/0032-0633(77)90055-1

Katoh, Y. (2014). A simulation study of the propagation of whistler-mode chorus in the Earth's inner magnetosphere. *Earth Planets and Space*, *66*, 6. https://doi.org/10.1186/1880-5981-66-6

Katoh, Y., & Omura, Y. (2007). Computer simulation of chorus wave generation in the Earth's inner magnetosphere. *Geophysical Research Letters*, *34*, 3102. https://doi.org/10.1029/2006GL028594

Katoh, Y., & Omura, Y. (2016). Electron hybrid code simulation of whistler-mode chorus generation with real parameters in the Earth's inner magnetosphere. *Earth Planets and Space*, *68*(1), 192. https://doi.org/10.1186/s40623-016-0568-0

Kennel, C. F. (1966). Low-frequency whistler mode. *Physics of Fluids*, *9*, 2190–2202. https://doi.org/10.1063/1.1761588

Kennel, C. F., & Petschek, H. E. (1966). Limit on stably trapped particle fluxes. *Journal of Geophysical Research*, *71*, 1–28. https://doi.org/10.1029/jz071i001p00001

Khazanov, G. V., Robinson, R. M., Zesta, E., Sibeck, D. G., Chu, M., & Grubbs, G. A. (2018). Impact of precipitating electrons and magnetosphere-ionosphere coupling processes on ionospheric conductance. *Space Weather*, *16*(7), 829–837. https://doi.org/10.1029/2018SW001837

Khazanov, G. V., Tel'nikhin, A. A., & Kronberg, T. K. (2014). Stochastic electron motion driven by space plasma waves. *Nonlinear Processes in Geophysics*, *21*(1), 61–85. https://doi.org/10.5194/npg-21-61-2014

Khotyaintsev, Y. V., Cully, C. M., Vaivads, A., André, M., & Owen, C. J. (2011). Plasma jet braking: Energy dissipation and nonadiabatic electrons. *Physical Review Letters*, *106*(16), 165001. https://doi.org/10.1103/PhysRevLett.106.165001

Krafft, C., & Volokitin, A. S. (2018). Whistler envelope solitons. I. Dynamics in inhomogeneous plasmas. *Physics of Plasmas*, *25*(10), 102301. https://doi.org/10.1063/1.5041055

Le Contel, O., Roux, A., Jacquey, C., Robert, P., Berthomier, M., Chust, T., et al. (2009). Quasi-parallel whistler mode waves observed by THEMIS during near-Earth dipolarizations. *Annales Geophysicae*, *27*, 2259–2275. https://doi.org/10.5194/angeo-27-2259-2009

Le Contel, O., Roux, A., Robert, P., Coillot, C., Bouabdellah, A., de La Porte, B., et al. (2008). First results of the THEMIS search coil magnetometers. *Space Science Reviews*, *141*, 509–534. https://doi.org/10.1007/s11214-008-9371-y

Lichtenberg, A. J., & Lieberman, M. A. (1983). *Regular and stochastic motion*. Springer.

Li, W., & Hudson, M. K. (2019). Earth'sVan Allen radiation belts: From discovery to the Van Allen Probes era. *Journal of Geophysical Research: Space Physics*, *124*(11), 8319–8351. https://doi.org/10.1029/2018JA025940

Liu, J., Angelopoulos, V., Runov, A., & Zhou, X.-Z. (2013). On the current sheets surrounding dipolarizing flux bundles in the magnetotail: The case for wedgelets. *Journal of Geophysical Research: Space Physics*, *118*, 2000–2020. https://doi.org/10.1002/jgra.50092

Liu, J., Angelopoulos, V., Zhang, X.-J., Turner, D. L., Gabrielse, C., Runov, A., et al. (2016). Dipolarizing flux bundles in the cis-geosynchronous magnetosphere: Relationship between electric fields and energetic particle injections. *Journal of Geophysical Research: Space Physics*, *121*, 1362–1376. https://doi.org/10.1002/2015JA021691

Liu, J., Angelopoulos, V., Zhou, X.-Z., & Runov, A. (2014). Magnetic flux transport by dipolarizing flux bundles. *Journal of Geophysical Research: Space Physics*, *119*, 909–926. https://doi.org/10.1002/2013JA019395

Lotekar, A., Vasko, I. Y., Mozer, F. S., Hutchinson, I., Artemyev, A. V., Bale, S. D., et al. (2020). Multisatellite mms analysis of electron holes in the Earth's magnetotail: Origin, properties, velocity gap, and transverse instability. *Journal of Geophysical Research: Space Physics*, *125*(9), e2020JA028066. https://doi.org/10.1029/2020JA028066

Lu, S., Angelopoulos, V., & Fu, H. (2016). Suprathermal particle energization in dipolarization fronts: Particle-in-cell simulations. *Journal of Geophysical Research: Space Physice*, *121*, 9843–9500. https://doi.org/10.1002/2016JA022815

Lu, S., Artemyev, A. V., Angelopoulos, V., Lin, Y., Zhang, X. J., Liu, J., et al. (2019). The Hall electric field in Earth's magnetotail thin current sheet. *Journal of Geophysical Research: Space Physics*, *124*(2), 1052–1062. https://doi.org/10.1029/2018JA026202

Lukin, A. S., Artemyev, A. V., & Petrukovich, A. A. (2021). On application of stochastic differential equations for simulation of nonlinear wave-particle resonant interactions. *Physics of Plasmas*, *28*(9), 092904. https://doi.org/10.1063/5.0058054

Lukin, A. S., Artemyev, A. V., Petrukovich, A. A., & Zhang, X. J. (2021). Charged particle scattering in dipolarized magnetotail. arXiv e-prints, arXiv:2105.05397.

Lyons, L. R. (1984). Electron energization in the geomagnetic tail current sheet. *Journal of Geophysical Research*, *89*, 5479–5487. https://doi.org/10.1029/JA089iA07p05479

Lyons, L. R., Thorne, R. M., & Kennel, C. F. (1972). Pitch-angle diffusion of radiation belt electrons within the plasmasphere. *Journal of Geophysical Research*, *77*, 3455–3474. https://doi.org/10.1029/JA077i019p03455

Lyons, L. R., & Williams, D. J. (1984). *Quantitative aspects of magnetospheric physics*. Springer.

Malykhin, A. Y., Grigorenko, E. E., Shklyar, D. R., Panov, E. V., Le Contel, O., Avanov, L., & Giles, B. (2021). Characteristics of resonant electrons interacting with whistler waves in the nearest dipolarizing magnetotail. *Journal of Geophysical Research: Space Physics*, *126*(7), e29440. https://doi.org/10.1029/2021JA029440

McFadden, J. P., Carlson, C. W., Larson, D., Ludlam, M., Abiad, R., Elliott, B., et al. (2008). The THEMIS ESA plasma instrument and in-flight calibration. *Space Science Reviews*, *141*, 277–302. https://doi.org/10.1007/s11214-008-9440-2

Michael, A., Sorathia, K., Ukhorskiy, A. Y., Albert, J., Shen, X., Li, W., et al. (2021). *The role of whistler chorus waves in rapid Buildup of radiation belt Intensities in Storm Recovery phase: Global test-particle simulations* (SM25A-08). AGU Fall Meeting Abstracts.

Morozov, A. I., & Solov'ev, L. S. (1966). Motion of charged particles in electromagnetic fields. *Reviews of plasma physics*, *2*, 201–297.

Motoba, T., Ohtani, S., Gkioulidou, M., Mitchell, D. G., Ukhorskiy, A. Y., Takahashi, K., et al. (2020). Pitch angle dependence of electron and ion flux changes during local magnetic dipolarization inside geosynchronous orbit. *Journal of Geophysical Research: Space Physics*, *125*(2), e27543. https://doi.org/10.1029/2019JA027543

Mourenas, D., Artemyev, A. V., Agapitov, O. V., & Krasnoselskikh, V. (2014). Consequences of geomagnetic activity on energization and loss of radiation belt electrons by oblique chorus waves. *Journal of Geophysical Research: Space Physics*, *119*, 2775–2796. https://doi.org/10.1002/2013JA019674

Mourenas, D., Artemyev, A. V., Ripoll, J.-F., Agapitov, O. V., & Krasnoselskikh, V. V. (2012). Timescales for electron quasi-linear diffusion by parallel and oblique lower-band Chorus waves. *Journal of Geophysical Research: Space Physics*, *117*, A06234. https://doi.org/10.1029/2012JA017717

Mourenas, D., Artemyev, A. V., Zhang, X. J., Angelopoulos, V., Tsai, E., & Wilkins, C. (2021). Electron lifetimes and diffusion rates inferred from ELFIN measurements at low altitude: First results. *Journal of Geophysical Research: Space Physics*, *126*(11), e29757. https://doi.org/10.1029/2021JA029757

Mozer, F. S., Agapitov, O., Artemyev, A., Drake, J. F., Krasnoselskikh, V., Lejosne, S., & Vasko, I. (2015). Time domain structures: What and where they are, what they do, and how they are made. *Geophysical Research Letters*, *42*, 3627–3638. https://doi.org/10.1002/2015GL063946

Nakamura, R., Baumjohann, W., Klecker, B., Bogdanova, Y., Balogh, A., Rème, H., et al. (2002). Motion of the dipolarization front during a flow burst event observed by Cluster. *Geophysical Research Letters*, *29*(20), 200000-1. https://doi.org/10.1029/2002GL015763

Nakamura, R., Baumjohann, W., Mouikis, C., Kistler, L. M., Runov, A., Volwerk, M., et al. (2004). Spatial scale of high-speed flows in the plasma sheet observed by Cluster. *Geophysical Research Letters*, *31*, 9804. https://doi.org/10.1029/2004GL019558

Nakamura, R., Retinò, A., Baumjohann, W., Volwerk, M., Erkaev, N., Klecker, B., et al. (2009). Evolution of dipolarization in the near-Earth current sheet induced by Earthward rapid flux transport. *Annales Geophysicae*, *27*, 1743–1754. https://doi.org/10.5194/angeo-27-1743-2009

Neishtadt, A. I. (1975). Passage through a separatrix in a resonance problem with a slowly-varying parameter. *Journal of Applied Mathematics and Mechanics*, *39*, 594–605. https://doi.org/10.1016/0021-8928(75)90060-X

Neishtadt, A. I. (1984). The separation of motions in systems with rapidly rotating phase. *Journal of Applied Mathematics and Mechanics*, *48*, 133–139. https://doi.org/10.1016/0021-8928(84)90078-9

Neishtadt, A. I. (1999). On adiabatic invariance in two-frequency systems. In C.Simo (Ed.), *Hamiltonian systems with three or more degrees of freedom* (NATO ASI Series C, Vol. 533, pp. 193–213). Kluwer Academic Publishers. https://doi.org/10.1063/1.166236

Neishtadt, A. I. (2000). On the accuracy of persistence of adiabatic invariant in single-frequency system. *Regular & Chaotic Dynamics*, *5*, 213–218. https://doi.org/10.1070/RD2000v005n02ABEH000143

Neishtadt, A. I., & Artemyev, A. V. (2020). Hamiltonian in guiding center theory: A symplectic structure approach. *Proceedings of the Steklov Institute of Mathematics*, *310*, 214–219. https://doi.org/10.1134/s008154382005017x

Neishtadt, A. I., & Vasiliev, A. A. (2006). Destruction of adiabatic invariance at resonances in slow fast Hamiltonian systems. *Nuclear Instruments and Methods in Physics Research*, *561*, 158–165. https://doi.org/10.1016/j.nima.2006.01.008

Ni, B., Liang, J., Thorne, R. M., Angelopoulos, V., Horne, R. B., Kubyshkina, M., et al. (2012). Efficient diffuse auroral electron scattering by electrostatic electron cyclotron harmonic waves in the outer magnetosphere: A detailed case study. *Journal of Geophysical Research*, *115*, A01218. https://doi.org/10.1029/2011JA017095

Ni, B., Thorne, R. M., Meredith, N. P., Horne, R. B., & Shprits, Y. Y. (2011). Resonant scattering of plasma sheet electrons leading to diffuse auroral precipitation: 2. Evaluation for whistler mode chorus waves. *Journal of Geophysical Research*, *116*, A04219. https://doi.org/10.1029/2010JA016233

Ni, B., Thorne, R. M., Shprits, Y. Y., Orlova, K. G., & Meredith, N. P. (2011). Chorus-driven resonant scattering of diffuse auroral electrons in nondipolar magnetic fields. *Journal of Geophysical Research: Space Physics*, *116*, 6225. https://doi.org/10.1029/2011JA016453

Ni, B., Thorne, R. M., Zhang, X., Bortnik, J., Pu, Z., Xie, L., et al. (2016). Origins of the earth's diffuse auroral precipitation. *Space Science Reviews*, *200*, 205–259. https://doi.org/10.1007/s11214-016-0234-7

Nishimura, Y., Lessard, M. R., Katoh, Y., Miyoshi, Y., Grono, E., Partamies, N., et al. (2020). Diffuse and pulsating aurora. *Space Science Reviews*, *216*(1), 4. https://doi.org/10.1007/s11214-019-0629-3

Northrop, T. G. (1963). *The adiabatic motion of charged particles*. John Wiley.

Nunn, D. (1974). A self-consistent theory of triggered VLF emissions. *Planetary and Space Science*, *22*, 349–378. https://doi.org/10.1016/0032-0633(74)90070-1

Nunn, D., Santolik, O., Rycroft, M., & Trakhtengerts, V. (2009). On the numerical modelling of VLF chorus dynamical spectra. *Annales Geophysicae*, *27*, 2341–2359. https://doi.org/10.5194/angeo-27-2341-2009

Omura, Y. (2021). Nonlinear wave growth theory of whistler-mode chorus and hiss emissions in the magnetosphere. *Earth Planets and Space*, *73*(1), 95. https://doi.org/10.1186/s40623-021-01380-w

Omura, Y., Furuya, N., & Summers, D. (2007). Relativistic turning acceleration of resonant electrons by coherent whistler mode waves in a dipole magnetic field. *Journal of Geophysical Research: Space Physics*, *112*, 6236. https://doi.org/10.1029/2006JA012243

Omura, Y., Miyashita, Y., Yoshikawa, M., Summers, D., Hikishima, M., Ebihara, Y., & Kubota, Y. (2015). Formation process of relativistic electron flux through interaction with chorus emissions in the Earth's inner magnetosphere. *Journal of Geophysical Research: Space Physics*, *120*, 9545–9562. https://doi.org/10.1002/2015JA021563

Omura, Y., Nunn, D., & Summers, D. (2013). Generation processes of whistler mode chorus emissions: Current status of nonlinear wave growth theory. In D.Summers, I. U.Mann, D. N.Baker, & M.Schulz (Eds.), *Dynamics of the Earth's radiation belts and inner magnetosphere* (pp. 243–254). American Geophysical Union. https://doi.org/10.1029/2012GM001347

Panov, E. V., Artemyev, A. V., Baumjohann, W., Nakamura, R., & Angelopoulos, V. (2013). Transient electron precipitation during oscillatory BBF braking: THEMIS observations and theoretical estimates. *Journal of Geophysical Research: Space Physics*, *118*, 3065–3076. https://doi.org/10.1002/jgra.50203

Runov, A., Angelopoulos, V., Gabrielse, C., Liu, J., Turner, D. L., & Zhou, X.-Z. (2015). Average thermodynamic and spectral properties of plasma in and around dipolarizing flux bundles. *Journal of Geophysical Research: Space Physics*, *120*, 4369–4383. https://doi.org/10.1002/2015JA021166

Runov, A., Angelopoulos, V., Gabrielse, C., Zhou, X.-Z., Turner, D., & Plaschke, F. (2013). Electron fluxes and pitch-angle distributions at dipolarization fronts: THEMIS multipoint observations. *Journal of Geophysical Research: Space Physics*, *118*, 744–755. https://doi.org/10.1002/jgra.50121

Runov, A., Angelopoulos, V., Sitnov, M. I., Sergeev, V. A., Bonnell, J., McFadden, J. P., et al. (2009). THEMIS observations of an earthward-propagating dipolarization front. *Geophysical Research Letters*, *36*, L14106. https://doi.org/10.1029/2009GL038980

Runov, A., Angelopoulos, V., Sitnov, M., Sergeev, V. A., Nakamura, R., Nishimura, Y., et al. (2011). Dipolarization fronts in the magnetotail plasma sheet. *Planetary and Space Science*, *59*, 517–525. https://doi.org/10.1016/j.pss.2010.06.006

Runov, A., Angelopoulos, V., Zhou, X.-Z., Zhang, X.-J., Li, S., Plaschke, F., & Bonnell, J. (2011). A THEMIS multicase study of dipolarization fronts in the magnetotail plasma sheet. *Journal of Geophysical Research*, *116*, 5216. https://doi.org/10.1029/2010JA016316

Runov, A., Sergeev, V. A., Nakamura, R., Baumjohann, W., Apatenkov, S., Asano, Y., et al. (2006). Local structure of the magnetotail current sheet: 2001 cluster observations. *Annales Geophysicae*, *24*, 247–262. https://doi.org/10.5194/angeo-24-247-2006

Sagdeev, R. Z., & Shafranov, V. D. (1961). On the instability of a plasma with an anisotropic distribution of velocities in a magnetic field. *Soviet Physics Journal of Experimental and Theoretical Physics*, *12*(1), 130–132. Retrieved from http://www.jetp.ras.ru/cgi-bin/dn/e_012_01_0130.pdf

Schindler, K. (1975). Plasma and fields in the magnetospheric tail. *Space Science Reviews*, *17*, 589–614. https://doi.org/10.1007/BF00718586

Schindler, K., & Birn, J. (1978). Magnetospheric physics. *Physics Report*, *47*, 109–165. https://doi.org/10.1016/0370-1573(78)90016-9

Schulz, M., & Lanzerotti, L. J. (1974). *Particle diffusion in the radiation belts*. Springer.

Sergeev, V. A., Gordeev, E. I., Merkin, V. G., & Sitnov, M. I. (2018). Does a local B-minimum appear in the tail current sheet during a substorm growth phase? *Geophysical Research Letters*, *45*, 2566–2573. https://doi.org/10.1002/2018GL077183

Sergeev, V. A., Nishimura, Y., Kubyshkina, M., Angelopoulos, V., Nakamura, R., & Singer, H. (2012). Magnetospheric location of the equatorward prebreakup arc. *Journal of Geophysical Research*, *117*(A1), A01212. https://doi.org/10.1029/2011JA017154

Sergeev, V. A., Pellinen, R. J., & Pulkkinen, T. I. (1996). Steady magnetospheric convection: A review of recent results. *Space Science Reviews*, *75*, 551–604. https://doi.org/10.1007/BF00833344

Shapiro, V. D., & Sagdeev, R. Z. (1997). Nonlinear wave-particle interaction and conditions for the applicability of quasilinear theory. *Physics Reports*, *283*, 49–71. https://doi.org/10.1016/S0370-1573(96)00053-1

Shen, Y., Artemyev, A., Zhang, X.-J., Vasko, I. Y., Runov, A., Angelopoulos, V., & Knudsen, D. (2020). Potential evidence of low-energy electron scattering and ionospheric precipitation by time domain structures. *Geophysical Research Letters*, *47*(16), e89138. https://doi.org/10.1029/2020GL089138

Shen, Y., Vasko, I. Y., Artemyev, A., Malaspina, D. M., Chu, X., Angelopoulos, V., & Zhang, X.-J. (2021). Realistic electron diffusion rates and lifetimes due to scattering by electron holes. *Journal of Geophysical Research: Space Physics*, *126*(9), e29380. https://doi.org/10.1029/2021JA029380

Shklyar, D. R. (1981). Stochastic motion of relativistic particles in the field of a monochromatic wave. *Soviet Physics Journal of Experimental and Theoretical Physics*, *53*, 1197–1192.

Shklyar, D. R. (2011). On the nature of particle energization via resonant wave-particle interaction in the inhomogeneous magnetospheric plasma. *Annales Geophysicae*, *29*, 1179–1188. https://doi.org/10.5194/angeo-29-1179-2011

Shklyar, D. R. (2017). Energy transfer from lower energy to higher-energy electrons mediated by whistler waves in the radiation belts. *Journal of Geophysical Research: Space Physics*, *122*(1), 640–655. https://doi.org/10.1002/2016JA023263

Shklyar, D. R., & Matsumoto, H. (2009). Oblique whistler-mode waves in the inhomogeneous magnetospheric plasma: Resonant interactions with energetic charged particles. *Surveys in Geophysics*, *30*, 55–104. https://doi.org/10.1007/s10712-009-9061-7

Shprits, Y. Y., & Ni, B. (2009). Dependence of the quasi-linear scattering rates on the wave normal distribution of chorus waves. *Journal of Geophysical Research: Space Physics*, *114*, 11205. https://doi.org/10.1029/2009JA014223

Shprits, Y. Y., Subbotin, D. A., Meredith, N. P., & Elkington, S. R. (2008). Review of modeling of losses and sources of relativistic electrons in the outer radiation belt II: Local acceleration and loss. *Journal of Atmospheric and Solar-Terrestrial Physics*, *70*, 1694–1713. https://doi.org/10.1016/j.jastp.2008.06.014

Shustov, P. I., Artemyev, A. V., & Yushkov, E. V. (2015). Intermediate regime of charged particle scattering in the field-reversal configuration. *Chaos*, *25*(12), 123118. https://doi.org/10.1063/1.4938535

Sitnov, M. I., Stephens, G., Motoba, T., & Swisdak, M. (2021). Data mining reconstruction of magnetotail reconnection and implications for its first-principle modeling. *Frontiers in Physics*, *9*, 90. https://doi.org/10.3389/fphy.2021.644884

Sitnov, M. I., Swisdak, M., & Divin, A. V. (2009). Dipolarization fronts as a signature of transient reconnection in the magnetotail. *Journal of Geophysical Research: Atmospheres*, *114*, A04202. https://doi.org/10.1029/2008JA013980

Slutskin, A. A. (1964). Motion of a one-dimensional nonlinear oscillator under adiabatic conditions. *Soviet Physics Journal of Experimental and Theoretical Physics*, *18*, 676–682. Retrieved from http://www.jetp.ras.ru/cgi-bin/dn/e_018_03_0676.pdf

Solovev, V. V., & Shkliar, D. R. (1986). Particle heating by a low-amplitude wave in an inhomogeneous magnetoplasma. *Soviet Physics Journal of Experimental and Theoretical Physics*, *63*, 272–277. Retrieved from https://ui.adsabs.harvard.edu/abs/1986ZhETF..90..471S/abstract

Sorathia, K. A., Ukhorskiy, A. Y., Merkin, V. G., Fennell, J. F., & Claudepierre, S. G. (2018). Modeling the depletion and recovery of the outer radiation belt during a geomagnetic storm: Combined MHD and test particle simulations. *Journal of Geophysical Research: Space Physics*, *123*(7), 5590–5609. https://doi.org/10.1029/2018JA025506

Spanswick, E., Donovan, E., Friedel, R., & Korth, A. (2007). Ground based identification of dispersionless electron injections. *Geophysical Research Letters*, *34*(3), L03101. https://doi.org/10.1029/2006GL028329

Stephens, G. K., Sitnov, M. I., Korth, H., Tsyganenko, N. A., Ohtani, S., Gkioulidou, M., & Ukhorskiy, A. Y. (2019). Global empirical picture of magnetospheric substorms inferred from multimission magnetometer data. *Journal of Geophysical Research: Space Physics*, *124*(2), 1085–1110. https://doi.org/10.1029/2018JA025843

Stern, D. P. (1970). Euler potentials. *American Journal of Physics*, *38*, 494–501. https://doi.org/10.1119/1.1976373

Stix, T. H. (1962). *The theory of plasma waves*. McGraw-Hill.

Su, T. (2012). On the accuracy of conservation of adiabatic invariants in slow-fast Hamiltonian systems. *Regular & Chaotic Dynamics*, *17*, 54–62. https://doi.org/10.1134/S1560354712010054

Summers, D., Ni, B., & Meredith, N. P. (2007). Timescales for radiation belt electron acceleration and loss due to resonant wave-particle interactions: 1. Theory. *Journal of Geophysical Research: Space Physics*, *112*, A04206. https://doi.org/10.1029/2006JA011801

Tao, X., Chan, A. A., Albert, J. M., & Miller, J. A. (2008). Stochastic modeling of multidimensional diffusion in the radiation belts. *Journal of Geophysical Research: Psace Physics*, *113*(A7), A07212. https://doi.org/10.1029/2007JA012985

Tao, X., Thorne, R. M., Li, W., Ni, B., Meredith, N. P., & Horne, R. B. (2011). Evolution of electron pitch angle distributions following injection from the plasma sheet. *Journal of Geophysical Research: Space Physics*, *116*, A04229. https://doi.org/10.1029/2010JA016245

Tao, X., Zonca, F., & Chen, L. (2017). Identify the nonlinear wave-particle interaction regime in rising tone chorus generation. *Geophysical Research Letters*, *44*(8), 3441–3446. https://doi.org/10.1002/2017GL072624

Tao, X., Zonca, F., & Chen, L. (2021). A "trap-release-amplify" model of chorus waves. *Journal of Geophysical Research: Space Physics*, *126*(9), e2021JA029585. https://doi.org/10.1029/2021JA029585

Tao, X., Zonca, F., Chen, L., & Wu, Y. (2020). Theoretical and numerical studies of chorus waves: A review. *Science China Earth Sciences*, *63*(1), 78–92. https://doi.org/10.1007/s11430-019-9384-6

Thorne, R. M., Bortnik, J., Li, W., & Ma, Q. (2021). Wave–particle interactions in the earth's magnetosphere. In R. Maggiolo, N. André, et al. (Eds.), *Magnetospheres in the solar system* (pp. 93–108). American Geophysical Union. https://doi.org/10.1002/9781119815624.ch6

Trakhtengerts, V. Y. (1963). The mechanism of generation of very low frequency electromagnetic radiation in the earth's outer radiation belt. *Geomagnetism and Aeronomy*, *3*, 365–371.

Tsyganenko, N. A. (1989). A magnetospheric magnetic field model with a warped tail current sheet. *Planetary and Space Science*, *37*, 5–20. https://doi.org/10.1016/0032-0633(89)90066-4

Tsyganenko, N. A. (1995). Modeling the Earth's magnetospheric magnetic field confined within a realistic magnetopause. *Journal of Geophysical Research: Space Physics*, *100*, 5599–5612. https://doi.org/10.1029/94JA03193

Tsyganenko, N. A., Andreeva, V. A., Sitnov, M. I., Stephens, G. K., Gjerloev, J. W., Chu, X., & Troshichev, O. A. (2021). Reconstructing substorms via historical data mining: Is it really feasible? *Journal of Geophysical Research: Space Physics*, *126*(10), e2021JA029604. https://doi.org/10.1029/2021JA029604

Tsyganenko, N. A., & Mukai, T. (2003). Tail plasma sheet models derived from Geotail particle data. *Journal of Geophysical Research*, *108*, 1136. https://doi.org/10.1029/2002JA009707

Tsyganenko, N. A., & Sitnov, M. I. (2007). Magnetospheric configurations from a high-resolution data-based magnetic field model. *Journal of Geophysical Research: Space Physics*, *112*, A06225. https://doi.org/10.1029/2007JA012260

Turner, D. L., Angelopoulos, V., Shprits, Y., Kellerman, A., Cruce, P., & Larson, D. (2012). Radial distributions of equatorial phase space density for outer radiation belt electrons. *Geophysical Research Letters*, *39*(9), L09101. https://doi.org/10.1029/2012GL051722

Turner, D. L., Fennell, J. F., Blake, J. B., Clemmons, J. H., Mauk, B. H., Cohen, I. J., et al. (2016). Energy limits of electron acceleration in the plasma sheet during substorms: A case study with the magnetospheric multiscale (mms) mission. *Geophysical Research Letters*, *43*(15), 7785–7794. https://doi.org/10.1002/2016GL069691

Tverskoy, B. A. (1969). Main mechanisms in the formation of the Earth's radiation belts. *Reviews of Geophysics and Space Physics*, *7*, 219–231. https://doi.org/10.1029/RG007i001p00219

Ukhorskiy, A. Y., Sitnov, M. I., Millan, R. M., & Kress, B. T. (2011). The role of drift orbit bifurcations in energization and loss of electrons in the outer radiation belt. *Journal of Geophysical Research*, *116*, A09208. https://doi.org/10.1029/2011JA016623

Vainchtein, D., Zhang, X. J., Artemyev, A. V., Mourenas, D., Angelopoulos, V., & Thorne, R. M. (2018). Evolution of electron distribution driven by nonlinear resonances with intense field-aligned chorus waves. *Journal of Geophysical Research: Space Physics*, *123*(10), 8149–8169. https://doi.org/10.1029/2018JA025654

Vasilev, A. A., Zaslavskii, G. M., Natenzon, M. I., Neishtadt, A. I., & Petrovichev, B. A. (1988). Attractors and stochastic attractors of motion in a magnetic field. *Zhurnal Eksperimental'noi i Teoreticheskoi Fiziki*, *94*, 170–187. Retrieved from https://ui.adsabs.harvard.edu/abs/1988ZhETF..94..170V/abstract

Vasko, I. Y., Agapitov, O. V., Mozer, F. S., & Artemyev, A. V. (2015). Thermal electron acceleration by electric field spikes in the outer radiation belt: Generation of field-aligned pitch angle distributions. *Journal of Geophysical Research: Space Physics*, *120*, 8616–8632. https://doi.org/10.1002/2015JA021644

Vasko, I. Y., Agapitov, O. V., Mozer, F. S., Bonnell, J. W., Artemyev, A. V., Krasnoselskikh, V. V., et al. (2017). Electron-acoustic solitons and double layers in the inner magnetosphere. *Geophysical Research Letters*, *44*, 4575–4583. https://doi.org/10.1002/2017GL074026

Vedenov, A. A., Velikhov, E., & Sagdeev, R. (1962). Quasilinear theory of plasma oscillations. *Nuclear Fusion*, *2*(Suppl), 465–475. Retrieved from https://www.osti.gov/biblio/4726983-quasi-linear-theory-plasma-oscillations

Wang, C., Lyons, L. R., Wolf, R. A., Nagai, T., Weygand, J. M., & Lui, A. T. Y. (2009). Plasma sheet $PV^{5/3}$ and nV and associated plasma and energy transport for different convection strengths and AE levels. *Journal of Geophysical Research*, *114*, A00D02. https://doi.org/10.1029/2008JA013849

Watt, C. E. J., Degeling, A. W., & Rankin, R. (2013). Constructing the frequency and wave normal distribution of whistler-mode wave power. *Journal of Geophysical Research: Space Physics*, *118*, 1984–1991. https://doi.org/10.1002/jgra.50231

Yahnin, A. G., Sergeev, V. A., Gvozdevsky, B. B., & Vennerstrøm, S. (1997). Magnetospheric source region of discrete auroras inferred from their relationship with isotropy boundaries of energetic particles. *Annales Geophysicae*, *15*, 943–958. https://doi.org/10.1007/s00585-997-0943-z

Young, S. L., Denton, R. E., Anderson, B. J., & Hudson, M. K. (2002). Empirical model for μ scattering caused by field line curvature in a realistic magnetosphere. *Journal of Geophysical Research: Space Physics*, *107*, 1069. https://doi.org/10.1029/2000JA000294

Young, S. L., Denton, R. E., Anderson, B. J., & Hudson, M. K. (2008). Magnetic field line curvature induced pitch angle diffusion in the inner magnetosphere. *Journal of Geophysical Research*, *113*, 3210. https://doi.org/10.1029/2006JA012133

Zaharia, S., Cheng, C. Z., & Johnson, J. R. (2000). Particle transport and energization associated with substorms. *Journal of Geophysical Research: Space Physics*, *105*, 18741–18752. https://doi.org/10.1029/1999JA000407

Zelenyi, L. M., Neishtadt, A. I., Artemyev, A. V., Vainchtein, D. L., & Malova, H. V. (2013). Quasiadiabatic dynamics of charged particles in a space plasma. *Physics-Uspekhi*, *56*, 347–394. https://doi.org/10.3367/UFNe.0183.201304b.0365

Zelenyi, L. M., Zogin, D. V., & Büchner, J. (1990). Quasiadiabatic dynamics of charged particles in the tail of the magnetosphere. *Cosmic Research*, *28*, 369–380.

Zhang, X., & Angelopoulos, V. (2014). On the relationship of electrostatic cyclotron harmonic emissions with electron injections and dipolarization fronts. *Journal of Geophysical Research: Space Physics*, *119*, 2536–2549. https://doi.org/10.1002/2013JA019540

Zhang, X., Angelopoulos, V., Artemyev, A. V., & Liu, J. (2018). Whistler and electron firehose instability control of electron distributions in and around dipolarizing flux bundles. *Geophysical Research Letters*, *45*, 9380–9389. https://doi.org/10.1029/2018GL079613

Zhang, X., Angelopoulos, V., Artemyev, A. V., & Liu, J. (2019). Energy transport by whistler waves around dipolarizing flux bundles. *Geophysical Research Letters*, *46*(21), 11718–11727. https://doi.org/10.1029/2019GL084226

Zhang, X., Angelopoulos, V., Artemyev, A. V., Zhang, X.-J., & Liu, J. (2021). Beam driven electron cyclotron harmonic waves in earth's magnetotail. *Journal of Geophysical Research: Space Physics*, *126*(3), e28743. https://doi.org/10.1029/2020JA028743

Zhang, X.-J., Angelopoulos, V., Ni, B., & Thorne, R. M. (2015). Predominance of ECH wave contribution to diffuse aurora in Earth's outer magnetosphere. *Journal of Geophysical Research: Space Physics*, *120*, 295–309. https://doi.org/10.1002/2014JA020455